Three-nucleon dynamics in *dp* breakup collisions at 190 MeV/nucleon using the WASA detector at COSY-Jülich

P. Adlarson,[1] W. Augustyniak,[2] W. Bardan,[3] M. Bashkanov,[4] F. S. Bergmann,[5] M. Berłowski,[6] A. Bondar,[7] M. Büscher,[8,9] H. Calén,[1] I. Ciepał,[10] H. Clement,[11,12] E. Czerwiński,[3] K. Demmich,[5] R. Engels,[13] A. Erven,[14] W. Eyrich,[15] P. Fedorets,[16] K. Föhl,[17] K. Fransson,[1] F. Goldenbaum,[13,*] A. Goswami,[13,18] K. Grigoryev,[13,*] L. Heijkenskjöld,[1,†] V. Hejny,[13] L. Jarczyk,[3,‡] T. Johansson,[1] B. Kamys,[3] G. Kemmerling,[14,§] A. Khoukaz,[5] A. Khreptak,[3] D. A. Kirillov,[19] S. Kistryn,[3] H. Kleines,[14,§] B. Kłos,[20,‖] W. Krzemień,[6] P. Kulessa,[10] A. Kupść,[1,6] K. Lalwani,[21] D. Lersch,[13,¶] B. Lorentz,[13,*] A. Magiera,[3] R. Maier,[13] P. Marciniewski,[1] B. Mariański,[2,‡] H.–P. Morsch,[2] P. Moskal,[3] W. Parol,[10] E. Perez del Rio,[3] N. M. Piskunov,[19] D. Prasuhn,[13] D. Pszczel,[1,6] K. Pysz,[10] J. Ritman,[13,22,*] A. Roy,[18] O. Rundel,[3] S. Sawant,[23] S. Schadmand,[13,*] T. Sefzick,[13,*] V. Serdyuk,[13] B. Shwartz,[7] T. Skorodko,[11,12] M. Skurzok,[3,**] J. Smyrski,[3] V. Sopov,[16,‡] R. Stassen,[13] J. Stepaniak,[6] E. Stephan,[20] G. Sterzenbach,[13] H. Stockhorst,[13] H. Ströher,[13] A. Szczurek,[10] A. Trzciński,[2,‡] M. Wolke,[1] A. Wrońska,[3] P. Wüstner,[14] A. Yamamoto,[24] J. Zabierowski,[25] M. J. Zieliński,[3] J. Złomańczuk,[1] P. Żuprański,[2] and M. Żurek[26]
(WASA-at-COSY Collaboration)[††]

A. Deltuva,[27] J. Golak,[3] A. Kozela,[10] A. Łobejko,[28] P. U. Sauer,[29] R. Skibiński,[3] I. Skwira-Chalot,[30] A. Wilczek,[20] and H. Witała[3]

[1]*Division of Nuclear Physics, Department of Physics and Astronomy, Uppsala University, Box 516, 75120 Uppsala, Sweden*
[2]*Nuclear Physics Division, National Centre for Nuclear Research, ul. Pasteura 7, 02-093 Warsaw, Poland*
[3]*M. Smoluchowski Institute of Physics, Jagiellonian University, prof. Stanisława Łojasiewicza 11, 30-348 Kraków, Poland*
[4]*School of Physics Engineering and Technology, The University of York, Heslington, York YO10 5DD, United Kingdom*
[5]*Institut für Kernphysik, Westfälische Wilhelms–Universität Münster, Wilhelm–Klemm–Str. 9, 48149 Münster, Germany*
[6]*High Energy Physics Division, National Centre for Nuclear Research, ul. Pasteura 7, 02-093 Warsaw, Poland*
[7]*Budker Institute of Nuclear Physics of SB RAS, 11 Acad. Lavrentieva Pr., Novosibirsk 630090, Russia*
[8]*Peter Grünberg Institut, PGI–6 Elektronische Eigenschaften, Forschungszentrum Jülich, 52425 Jülich, Germany*
[9]*Institut für Laser–und Plasmaphysik, Heinrich Heine Universität Düsseldorf, Universitätsstr. 1, 40225 Düsseldorf, Germany*
[10]*The Henryk Niewodniczański Institute of Nuclear Physics, Polish Academy of Sciences, ul. Radzikowskiego 152, 31-342 Kraków, Poland*
[11]*Physikalisches Institut, Eberhard Karls Universität Tübingen, Auf der Morgenstelle 14, 72076 Tübingen, Germany*
[12]*Kepler Center for Astro and Particle Physics, Physikalisches Institut der Universität Tübingen, Auf der Morgenstelle 14, 72076 Tübingen, Germany*
[13]*Institut für Kernphysik, Forschungszentrum Jülich, 52425 Jülich, Germany*
[14]*Zentralinstitut für Engineering, Elektronik und Analytik, Forschungszentrum Jülich, 52425 Jülich, Germany*
[15]*Physikalisches Institut, Friedrich–Alexander Universität Erlangen–Nürnberg, Erwin–Rommel-Str. 1, 91058 Erlangen, Germany*
[16]*National Research Centre "Kurchatov Institute," Moscow 123182, Russia*
[17]*II. Physikalisches Institut, Justus–Liebig–Universität Gießen, Heinrich–Buff–Ring 16, 35392 Giessen, Germany*
[18]*Discipline of Physics, Indian Institute of Technology Indore, Khandwa Road, Indore, Madhya Pradesh 453552, India*
[19]*Veksler and Baldin Laboratory of High Energiy Physics, Joint Institute for Nuclear Physics, 6 Joliot–Curie, Dubna 141980, Russia*
[20]*August Chełkowski Institute of Physics, University of Silesia, ul. 75 Pułku Piechoty 1, 41-500 Chorzów, Poland*
[21]*Department of Physics, Malaviya National Institute of Technology Jaipur, JLN Marg, Jaipur, Rajasthan 302017, India*
[22]*Institut für Experimentalphysik I, Ruhr–Universität Bochum, Universitätsstr. 150, 44780 Bochum, Germany*
[23]*Department of Physics, Indian Institute of Technology Bombay, Powai, Mumbai, Maharashtra 400076, India*
[24]*High Energy Accelerator Research Organisation KEK, Tsukuba, Ibaraki 305–0801, Japan*

[*]Present address: GSI Helmholtzzentrum für Schwerionenforschung GmbH, Planckstraße 1, 64291 Darmstadt, Germany.
[†]Present address: Institut für Kernphysik, Johannes Gutenberg Universität Mainz, Johann–Joachim–Becher Weg 45, 55128 Mainz, Germany.
[‡]Deceased.
[§]Present address: Jülich Centre for Neutron Science JCNS, Forschungszentrum Jülich, 52428 Jülich, Germany.
[‖]Contact author: barbara.klos@us.edu.pl
[¶]Present address: Department of Physics, Florida State University, 77 Chieftan Way, Tallahassee, FL 32306-4350, USA.
[**]Present address: INFN, Laboratori Nazionali di Frascati, Via E. Fermi, 40, 00044 Frascati (Roma), Italy.
[††]The author list reflects the once-existing composition of the WASA-at-COSY Collaboration, within which the data presented in this paper have been obtained.

 ©2026 American Physical Society

[25]*Astrophysics Division, National Centre for Nuclear Research, Box 447, 90-950 Łódź, Poland*
[26]*Physics Division, Argonne National Laboratory, 9700 S Cass Ave, Lemont, Illinois 60439, USA*
[27]*Institute of Theoretical Physics and Astronomy, Vilnius University, Saulėtekio al. 3, LT-10257 Vilnius, Lithuania*
[28]*Institute of Experimental Physics, Faculty of Mathematics, Physics and Informatics, University of Gdańsk, PL-80308 Gdańsk, Poland*
[29]*Institute for Theoretical Physics, Leibniz University Hannover, D-30167 Hannover, Germany*
[30]*Faculty of Physics, University of Warsaw, PL-02093 Warszawa, Poland*

(Received 2 March 2026; revised 17 July 2026; accepted 21 September 2026; published 16 October 2026)

The differential cross section for the ^{1}H(d, pp)n breakup reaction at deuteron beam energy of 380 MeV has been determined with high statistical precision for 189 angular configurations of outgoing protons in the region of forward laboratory angles. The cross-section data were compared to theoretical predictions based on the state-of-the-art nucleon-nucleon potentials, combined with a three-nucleon force, the Coulomb interaction or carried out in a relativistic approach. In the region of the lowest differential cross section, the discrepancy between the data and the theoretical predictions is observed, also in the case of relativistic calculations.

DOI: 10.1103/k3z6-gvpd

I. INTRODUCTION

Properties of nuclei at medium energies are determined to a large extent by pairwise nucleon-nucleon (*NN*) interactions, which are a dominant component of the nuclear potential. However, neglecting internal degrees of freedom of interacting nucleons, it is necessary to introduce the many-body forces, in particular the three-nucleon force (3NF). State-of-the-art models of 3NF's, like TM99 [1], Urbana IX [2], or Illinois [3], combined with the realistic nucleon-nucleon (2N) potentials, constitute the basis for calculations of binding energies and scattering observables. Chiral effective field theory (ChEFT) provides a systematic construction of nuclear forces in a fully consistent way: The 3N forces appear naturally at a certain order [4,5]. The theoretical calculations including semiphenomenological 3NF or 3NF stemming from ChEFT reproduce with high accuracy binding energies of light nuclei; see Refs. [6–8] and references therein.

A comprehensive description of nuclear forces requires an accurate understanding of the few-nucleon systems. In particular, the three-nucleon system is the simplest to test the interaction models and constrain the 3NF parameters. It was demonstrated that by including 3NF the description of the differential cross section for elastic nucleon-deuteron scattering is significantly improved compared to calculations based only on *NN* interactions [9–11]. The remaining discrepancy between the data and theoretical calculations appears above 100 MeV/nucleon and has not been explained by either the influence of Coulomb interactions or relativistic effects, both of which are predicted to be small and very local. Studies of the ^{1}H(d, pp)n and ^{2}H(p, pp)n breakup reactions make an important contribution to investigations of the 3NF. The advantage relies on the kinematic richness of the three-body final state. There are experimental evidences of significant 3NF contributions to the differential cross section for the breakup reaction, already starting at a relatively low beam energy of 65 MeV/nucleon [12,13]. In contrast to the elastic scattering case, in the breakup reaction the Coulomb interaction is a very important component of dynamics. The Coulomb interaction between protons modifies the cross-section data over a significant part of the phase space, in particular at forward laboratory angles of the ^{1}H(d, pp)n reaction [14–16]. At present, the Coulomb interaction and 3N forces are both included in theoretical calculations and their interplay can be studied [17–19].

Relativistic calculations of the differential cross section for the breakup reaction led to different results than nonrelativistic ones [20]. Due to the significant predicted 3NF and relativistic effects in the energy region between 150 and 200 MeV/nucleon [20,21], the question arises of their interplay. So far, no calculations have been performed that treat in a fully relativistic way both the *NN* and 3NF interactions. Under such circumstances one has to rely on systematic (in beam energy) studies over large phase space regions, with the aim to single out both contributions on the basis of their different kinematic dependencies.

The very limited experimental dataset in this range, especially when it comes to data covering wide ranges of phase space, became the motivation for the experiments described here. The exception, a measurement of the ^{2}H(p, pp)n reaction at 190 MeV [22–24], provided hints of deficiencies in the description of the cross section for the deuteron breakup reaction, even when 3NF is included. The problem can be interpreted either as confirmation of the above-mentioned issues in elastic scattering or as a consequence of relativistic effects. The data presented in this work were taken in the inverse kinematics, ^{1}H(d, pp)n, complementing the studied region of the reaction phase space. They were part of a systematic study conducted with the Wide Angle Shower Apparatus (WASA) detector at COSY beam in the energy range from 150 to 200 MeV/nucleon, of which data at 170 MeV/nucleon have been published so far [25].

II. EXPERIMENT AND DATA ANALYSIS

An experiment to investigate the ^{1}H(d, pp)n breakup reaction using a deuteron beam of 150, 170, 190, 200 MeV/nucleon was performed in January 2013 at the Cooler Synchrotron COSY-Jülich. Energies 170, 190, and 200 MeV/nucleon of the deuteron beam were changed in a supercycle mode of time length 30 s, while measurement at 150 MeV/nucleon was performed separately. Due to the

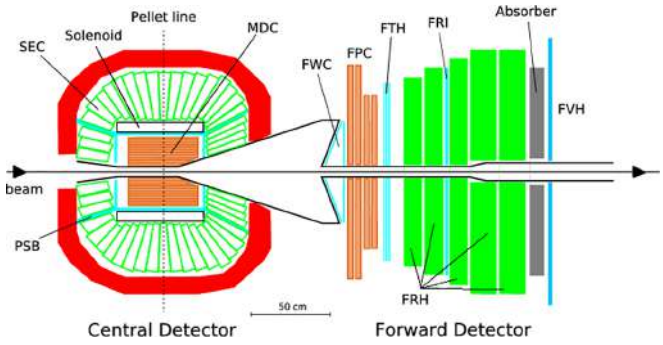

FIG. 1. Schematic view of the detection system.

acceptance close to 4π and the moderate detection threshold of the WASA detection system, differential cross-section data have been collected in a large part of the breakup reaction phase space. In this paper, the results of an analysis of the data collected at the beam energy of 190 MeV/nucleon are shown, with focus on the proton-proton coincidences registered in the Forward Detector.

A. WASA detector

The WASA detector [26,27] (see Fig. 1) consisted of four main components: the Central Detector (CD), Forward Detector (FD), Pellet Target, and Scattering Chamber. The pellet target provided a narrow stream of frozen hydrogen droplets. The Central Detector operated in the experiment described here, but the present data analysis is limited to the registration of protons and deuterons only in the Forward Detector.

FD consisted of a set of detectors for the identification of charged hadrons and track reconstruction: Forward Window Counter, Forward Proportional Chamber (FPC) and plastic scintillators: Forward Trigger Hodoscope, Forward Range Hodoscope (FRH) and Forward Veto Hodoscope. FPC was used for precise determination of particle emission angles. The FD plastic scintillators were used for particle identification and particle energy measurement. They all provided information for the first-level trigger logic; for details see Ref. [25]. Between the second (FRH2) and third (FRH3) layers of FRH there were two layers of Forward Range Interleaving Hodoscope (FRI). In addition, between the layers FRH3 and FRH4, a passive aluminum layer was placed to extend the energy range of particles stopped in the WASA detector not shown in Fig. 1).

B. Data analysis

The data analysis presented in this work was focused on proton-proton coincidences from the ^{1}H$(d, pp)n$ breakup reaction at 190 MeV/nucleon, registered in the Forward Detector. This was a follow-up of the analysis performed for data collected at 170 MeV/nucleon, described in detail in Ref. [25], thus the data analysis procedures were similar. Below we will present the main steps and focus on describing the differences associated with the different range of energies of particles in the exit channel. The multilayer structure of the Forward detector had a significant impact on the analysis procedures: As the energy of the outgoing particles increased, more layers were involved in the track reconstruction, which affected both energy calibration and detection efficiency.

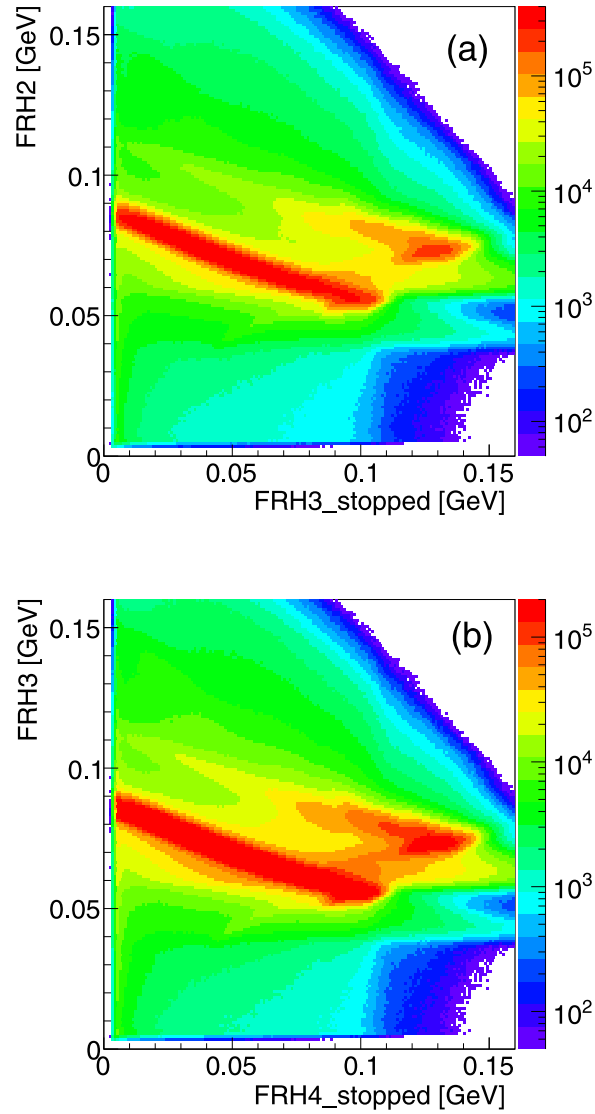

FIG. 2. Particle identification spectra of particles stopped in (a) third layer and (b) fourth layer of FRH. Loci of protons and deuterons are clearly visible.

In the first step of analysis, events of interest were selected: two protons from the breakup process and deuterons from elastic scattering channel, the latter used for the cross-section normalization. The particle identification was based on the ΔE–E_R technique, where E_R was the remaining energy deposit in the layer where the particle was stopped and ΔE denoted the energy deposit in the preceding layer. In the entire range of energies, a clear separation between loci of protons and deuterons was observed; see examples in Fig. 2.

1. Analysis of breakup events

The breakup configuration was defined by the emission angles of the two outgoing protons: two polar angles θ_1 and θ_2 (with $\theta_1 \leqslant \theta_2$), between 5 and 15°, and their relative azimuthal angle φ_{12}. The data were integrated over the angular ranges of

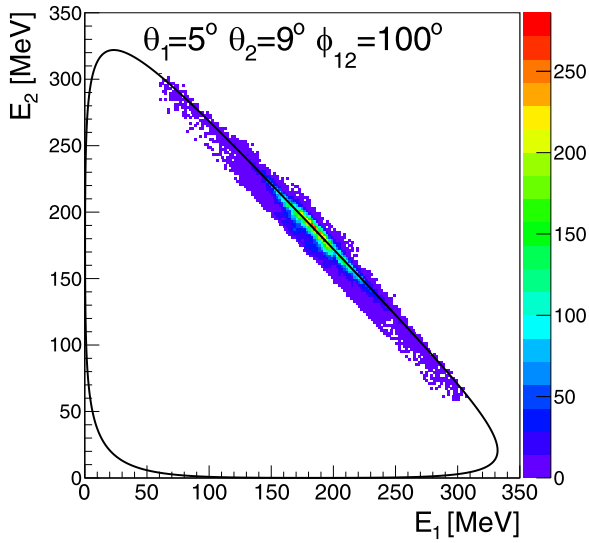

FIG. 3. E_1 vs E_2 coincidence spectrum of the two protons registered at $\theta_1 = 5^\circ \pm 1^\circ$, $\theta_2 = 9^\circ \pm 1^\circ$, and $\varphi_{12} = 100^\circ \pm 5^\circ$. The solid line shows a three-body kinematical curve, calculated for the central values of experimental angular ranges.

$\theta_{1,2}$ ($\pm 1^\circ$) and φ_{12} ($\pm 5^\circ$). In order to reduce the background, cut on neutron peak in the missing mass spectrum [28] was applied. For each angular configuration, the data were placed in a kinematic spectrum showing the energy correlation of the proton pair, E_1 versus E_2 (see Fig. 3), and then transformed to the variable S, which shows the position along the kinematical curve [25]. The starting point of the S curve ($S = 0$) is chosen as a point for which energy of the second proton is minimal. This step required precise energy calibration, which was based on measurements of dp elastic scattering at energies corresponding to minimum ionization [29]. Since the FRI detector was not used in a number of previous runs, its calibration was not included in the main calibration procedure and was known with lower accuracy. As in the analysis of the data collected at the beam energy of 170 MeV/nucleon [25], the appropriate corrections have been applied on the basis of energy deposited in the previous layer. This procedure has slightly deteriorated the energy resolution. Since the affected energy region corresponded to slopes of the cross section S distributions where energy reconstruction errors could have a significant impact on the result [28], thus an adequately wide binning in S of 24 MeV was applied. A similar issue arose for particles stopped in the aluminum layer between FRH3 and FRH4, but its impact on the reconstructed energy was much more pronounced due to the considerable thickness of this passive layer. Since it affected only the tails of the S distributions, it was decided to discard these regions, which only slightly limited S ranges of the cross-section data. The data presented in this paper are therefore limited to the regions where energy reconstruction is not affected by the aluminium layer.

The energy calibration was validated by the corelation of proton energies in each of the studied breakup configurations (see example in Fig. 3) and by reproduction of the neutron missing mass, for details see Ref. [28].

A WASA Monte Carlo program based on the Geant 3 simulation package was used for precise determination of efficiency of the detection system. The analysis of generated data included the detector acceptance and all cuts applied in the analysis. The efficiency for registering and identifying elastically scattered deuterons was determined for each polar angle and typically reached about 80%. The efficiency for proton-proton coincidences was determined for each kinematical configuration with defined integration limits: $\Delta\theta_1 = \Delta\theta_2 = 2^\circ$ and $\Delta\varphi_{12} = 10^\circ$. Differently from the analysis performed at lower beam energy [25], a common efficiency factor did not apply for the entire S range. This was due to the difference in the number of detector layers penetrated by coincident protons which depended on their energy. Therefore, for each configuration, the efficiency was determined on the basis of MC simulation, separately for the central part of S where both proton energies were below 210 MeV and for the rest of the studied range of the S distribution. In the central part of the S distribution, typical efficiency for registering breakup coincidences was 60%, while on the tails, it was reduced down to 50% due to one proton penetrating to the FRH3 layer [28]. The efficiency corrections obtained in this way were applied to the relevant S regions of the individual kinematic configurations.

2. Luminosity

The absolute normalization was derived from the luminosity determined on the basis of the number of elastically scattered deuterons. Deuterons were sorted with respect to their laboratory scattering angles, between 8° and 14° in a step of 1°. To remove the tail associated with hadronic interactions, limits were set on the deuteron peak in the corresponding energy spectra. After correcting for efficiency, the resulting number of deuterons recorded at each angle was obtained. The uncertainties associated with these values were determined by varying the cuts used in the data analysis and the MC simulations. To obtain an integrated luminosity, a number of deuterons registered at each angle was normalized to the known elastic scattering cross section at this angle.

Due to the considerable scatter of existing experimental data for deuteron-proton elastic scattering at the intermediate energies and very few measurements in an energy range similar to that of the study, several strategies were applied to obtain these normalization factors, similarly as in Ref. [25]. First, a fit to the data covering a wide range of beam energies was pursued. In the current analysis we also used the fact, that the angular range of elastically scattered deuterons corresponds to $\theta^p_{\mathrm{c.m.}} < 50^\circ$, which is a region of a so-called soft-scattering. In the elastic scattering, a part of the momentum and energy is transferred from the beam to the target, thus the square of the four-momentum transfer $t < 0$, and it can be described by

$$t = -2\mathrm{p}^{*2}c^2(1 - \cos\theta_{\mathrm{c.m.}}), \tag{1}$$

where p* corresponds to the momentum and $\theta_{\mathrm{c.m.}}$ denoting the beam particle scattering angle in the center-of-mass system. A four-momentum transfer defined as $qc = \sqrt{-t}$ is related to the momentum transferred to the target and reflects the "hardness" of the collision. The soft collisions mentioned above are

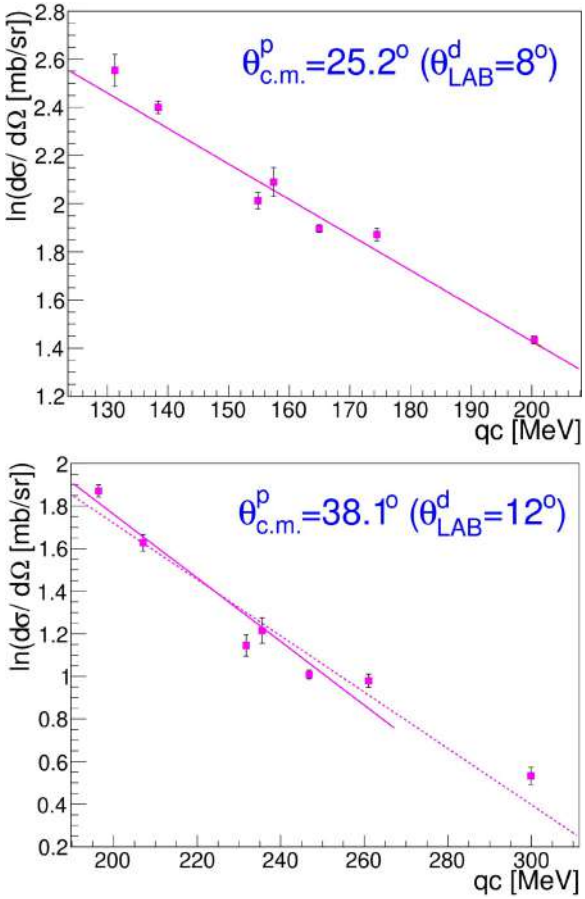

FIG. 4. Experimental differential cross section of the deuteron-proton elastic scattering at the incident-beam energies: 108, 120, 150, 170, 190 [31,32], 155 [33], and 250 MeV [10] presented as $\ln(\sigma)$ in a function of q for two scattering angles, specified in the panels. Two lines in the lower panel show linear fits including (dashed line) or excluding (solid line) the last point corresponding to the highest beam energy of 250 MeV.

long-range collisions characterized by small q. This region is also called the *scaling region* and it is dominated by the direct term in the two-nucleon potential. Moreover, the dynamical part (after removing the phase-space factor) of the cross section predominately depends on the momentum transfer and has a very small dependence on the beam energy (for further discussion see Ref. [30]). The cross-section dependence on the momentum transfer has dominating exponential character. Indeed, for beam energies ranging between 108 and 250 MeV and momentum transfers $q < 280$ MeV/c, the $\ln\sigma_{\mathrm{CDB+TM99}}$ calculated with the CD-Bonn potential combined with the TM99 3NF reveal a linear dependence on q and only at $\theta_{\mathrm{c.m.}}$ exceeding 45° and for $q > 300$ MeV/c a small departure from linearity is observed. This validates the linear fit to the experimental data in the similar ranges. In Fig. 4, the available pd elastic cross-section data and the corresponding fits are shown for two deuteron scattering angles. The last data point on the lower graph shows, as expected, a deviation from the linear trend; it was therefore removed from the final fit (solid line), but the results obtained for the dashed line are included in the systematic uncertainty budget. Analogous fits

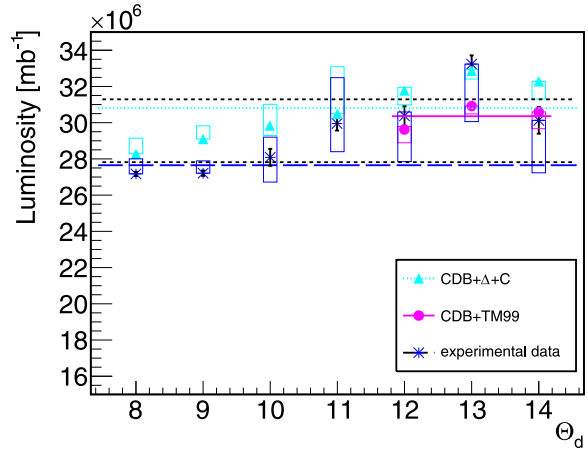

FIG. 5. Determination of the integrated luminosity. The integrated luminosity values were calculated independently for each deuteron scattering angle. Each set of points and corresponding average (horizontal line) corresponds to a different way of determining elastic scattering cross section used for normalization, as specified in the legend. Two additional dashed lines present the systematic uncertainty of the final result. For more details see the text.

provided the cross-section values for the beam energy under investigation at each deuteron exit angle. After applying these normalization factors, a series of integrated luminosity values was obtained; see the stars in Fig. 5.

Similarly to the previous analysis [25], these luminosity results were cross-checked with those based on theoretical calculations of the elastic scattering cross section. In the soft scattering region, the theoretical calculations including 3NF, for example CDB+Δ or CDB+TM99 (see Sec. III), provide an adequate description of the data. At the lowest q one should however take into account Coulomb interactions modifying the cross section. Therefore, two types of calculations were taken into account: the one including Coulomb, CDB+Δ+C, applicable in the full range of studied scattering angles, and CDB+TM99, to be used in the range of laboratory angles between 12° and 14° where the predicted Coulomb effects are below 2% (as stems from the comparison of the CDB+Δ+C and CDB+Δ predictions). The calculated cross-section values were used for determining integrated luminosity. The corresponding data points are shown as cyan triangles and magenta dots in Fig. 5, with previously mentioned experimental uncertainties. These results are compared to the earlier discussed luminosity values obtained with normalization to the fitted experimental cross sections (blue stars). In the latter case, uncertainties of the $\ln\sigma$ versus q fits were also included in the final uncertainty boxes. The spread of results within each of the methods illustrates differences of shapes of angular cross-section distributions obtained in this experiment and the corresponding normalization cross sections.

This spread sometimes exceeds the estimated systematic uncertainties of individual points. For each normalization method, the corresponding average was calculated, with weights that include systematic uncertainties (horizontal lines, as specified in the legend of Fig. 5). Analogously to the previous analysis [25], the result obtained with CDB+TM99

potential is taken as a luminosity value (horizontal solid magenta line in Fig. 5), and the other ones are used to determine systematic uncertainty. The systematic uncertainties marked as horizontal black dashed lines cover the range of scatter of individual data points obtained with all three normalization methods. Finally, the average integrated luminosity obtained for the full set of data is $(3.036 \pm 0.003) \times 10^7$ mb^{-1} with asymmetric systematic uncertainty of $(-0.254, +0.093) \times 10^7$ mb^{-1}, corresponding to a relative error of –8% and +3%.

3. *Experimental uncertainties*

Statistical uncertainties of the measured cross-section values comprise an uncertainty of the measured number of breakup coincidences and of the luminosity. In all 189 kinematic configurations statistical errors in peaks of the cross-section distributions are below 1%.

The data consistency checks and discussion of systematic uncertainties presented in Ref. [25] are valid also for the dataset presented here. The systematic uncertainties dominate over statistical ones and stem primarily from three sources:

(1) Luminosity determination, which affects the common normalization factor for all the data points. The systematic uncertainty of the integrated luminosity, as discussed in Sec. II B 2, is asymmetric, –8% and +3%, and thus leads to asymmetric uncertainty of the normalized cross section: –3% and +8%.
(2) Uncertainty of efficiency for detecting proton-proton coincidences. It corresponds to the accuracy of the MC simulations and consists of two parts: The systematic error of hadronic interaction modeling (7%) and the statistical accuracy of the simulations; the latter varies typically between 1% and 7% (only in 6 of 189 configurations it exceeds 7%).
(3) Background subtraction procedure; the corresponding uncertainty was determined for each data point in two ways: varying the range around the Gaussian peak where the linear background was determined and checking Gaussian shape of the distribution obtained after the background subtraction (by comparing the integral of the fitted Gauss with the sum of events); in the central parts of the *S* distributions it varies between 1 and 9%.

Finally, summing all the components in squares, we obtain systematic uncertainties ranging between 8 and 16% for the central regions of the studied *S* distributions, thus dominating over the statistical ones.

III. THEORETICAL CALCULATIONS

The experimental cross-section data measured at 190 MeV/nucleon have been compared to results of the same set of the calculations as in case of the earlier published data collected at 170 MeV/nucleon. The list of theoretical approaches is given in Table I; for details see Ref. [25] and references therein. To study the impact of individual contributions to system dynamics, a comparison was first made with

TABLE I. Definition of abbreviations applied for naming theoretical calculations. "aver" means averaging over angular ranges accepted in data analysis.

Abbreviation	Description	Aver	Reference
CDB	CD Bonn potential	Yes	[34,35]
CDB+TM99	CD Bonn potential combined with TM99 3NF	Yes	[1,36]
2N	Potentials: AV18, CD Bonn, Nijmegen I and II	Yes	[34,35,37,38]
2N+TM99	Potentials (as above) combined with TM99 3NF	Yes	[1,36]
CDB+Δ	Coupled-channels potential CD Bonn+explicit Δ	Yes	[39]
CDB+Δ+C	Coupled-channels potential CDB+Δ with Coulomb force	Yes	[17,18]
CDBrel	CD Bonn potential relativistic calculations	No	[21]

calculations based on pure *NN* potentials (2N and CDB in Table I). Next, the 3NF was taken into account (2N+TM99, CDB+Δ). The Coulomb interaction was applied to a purely nucleonic CDB potential (CDB+C) and its coupled-channels extension (CDB+Δ+C). In one case, CDBrel, the relativistic effects were taken into account. The group of calculations, CDB, CDB+TM99, 2N, 2N+TM99, and CDBrel, was performed by Witała *et al.*, while the second group, CDB, CDB+Δ, and CDB+Δ+C, was performed by Deltuva. As the CDB calculations were carried out by these two theoretical groups, we will refer to them as CDB (Witała) and CDB (Deltuva).

Prior to comparing with the data, the theoretical predictions were averaged over the same angular bins as used in the data analysis ($\Delta\theta_{1,2} = 2^\circ$, $\Delta\varphi_{12} = 10^\circ$) and projected onto relativistic kinematics; see Ref. [13]. The relativistic calculations are the only exception: The calculations were performed for central values of the angular ranges only. In other theoretical calculations, averaging changed the cross-section values by a few percentages. For example, in the case of configurations for which relativistic calculations were performed, shown in Fig. 6, the averaging effects for cross sections obtained with the CDB+Δ+C potential were contained in the range between –5% and +7% in the peaks. Despite the lack of averaging, comparison of the relativistic calculations with the data is still justified, with additional uncertainty of a few percentages.

The most extensive developments of nuclear potentials are nowadays carried out within the framework of ChEFT. It has been shown that with regard to *NN* interactions it is necessary to perform calculations at fifth order ($\nu = 5$), i.e., N4LO (see the discussion in Ref. [5]). Thus, the 3NF of the same order is required for consistency. So far, the complete calculations for Nd system at N3LO are unavailable and only approaches based on the realistic potentials are considered

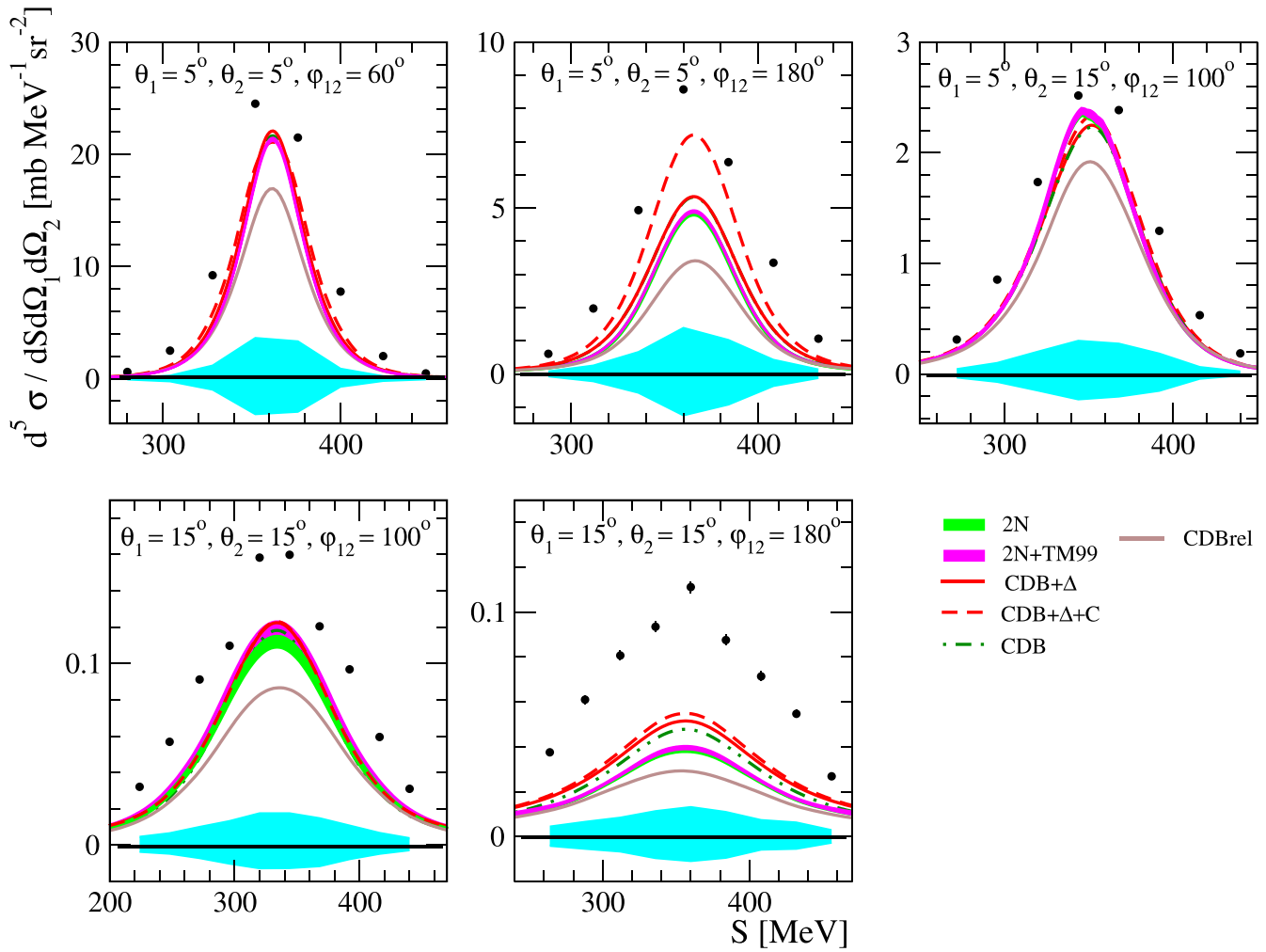

FIG. 6. Differential cross section of ^{1}H(d, pp)n breakup reaction at beam energy of 190 MeV/nucleon shown in a function of the S variable for the set of configurations specified in the panels. Bars representing statistical uncertainties are usually smaller than data points. Systematic uncertainties are represented by bands. Data are compared to theoretical calculations specified in the legend.

in this work. While work on completing 3NF at N3LO is underway, attempts have also been made to incorporate 3NF forces from the next order of chiral expansion. Specifically, the contributions of all subleading N4LO 3NF contact terms [40,41] to the elastic Nd scattering are discussed at low energies in Ref. [42] and up to $E = 250$ MeV in Ref. [43]. In the latter exploratory work the N3LO 3NF was omitted and the values of the two N2LO and 11 N4LO LECs were found using the solution of the Faddeev equation based on emulator [44,45]. The inclusion of the new components of the N4LO 3NF improves the description of some observables; however, the nucleon-deuteron scattering length disagrees with the experimental value. In Ref. [46] the cross section for the space-star breakup configuration was studied with the N4LO 3NF isoscalar central and spin-orbit interactions taken into account and the high sensitivity of the cross section to these terms was found at $E = 65$ MeV. However, the omission of N3LO 3NF in these calculations means their results should be treated with caution, and the studies themselves should be repeated with the complete 3NF as soon as it becomes available. Some other recent developments in calculating observables for the breakup reaction within ChEFT approach are also discussed in Ref. [8].

IV. RESULTS

The differential cross section for a regular grid of polar and azimuthal angles with a constant step in arclength variable S (24 MeV) was experimentally obtained. The polar angles of the two protons, θ_1 and θ_2, were changed between 5° and 15° with a step size of 2° and their relative azimuthal angle φ_{12} was analyzed in the range from 20° to 180°, with the step size of 20°. In total, 189 configurations have been analyzed.

Figure 6 presents cross-section distributions for the configurations for which relativistic calculations are available. This set can be considered representative for the phase space studied, with the smallest (5°) and largest (15°) among the analyzed polar angles, both symmetric and maximally asymmetric (respectively $\theta_2 - \theta_1 = 0°$ and 10°), combined with three very different relative azimuthal angles ($\varphi_{12} =$ 60°, 100°, and 180°). The data are compared to all the theoretical calculations listed in Table I. Theoretical bands

correspond to nonrelativistic 2N and 2N+TM99 calculations by Witała *et al*. and their width is related to differences between predictions obtained with individual *NN* potentials. Since the bands are narrow, further in quantitative analyses only CDB and CDB+TM99 will be used. The predicted 3NF effects are small or negligible. In all the cases shown in Fig. 6, relativistic calculations are significantly below both the nonrelativistic ones and the data and this difference exceeds by an order of magnitude the expected effect of averaging. In the top panels, a certain underestimation of the measured cross section by nonrelativistic theories is observed but roughly contained within systematic uncertainties. In one case ($\theta_1 = \theta_2 = 5^\circ$, $\varphi_{12} = 180^\circ$) the predicted Coulomb effect is significant and confirmed by the data.

The configurations shown in the bottom panels, with $\theta_1 = \theta_2 = 15^\circ$, are characterized by a very low cross section, one or two orders lower (in the peaks) than maximal cross-section values in the top panels. In these cases all the calculations significantly underestimate the experimental data. This confirms the findings from the measurement at 170 MeV/nucleon [25], though for the discussed currently data at 190 MeV/nucleon, discrepancies are even more pronounced, reaching a factor of 2 in the best case or even 4 in the case of the relativistic approach.

Figures 11–21 in Appendix A present the differential cross-section results for the full set of kinematic configurations studied. A brief review of them leads to similar qualitative conclusions to those presented above:

(1) The predicted 3NF effects are small in the entire angular region under study.
(2) Coulomb effects, as expected, dominate in the most forward configurations ($\theta_1, \theta_2 = 5^\circ$ or 7°) with the lowest ($\varphi_{12} = 20^\circ$) and highest ($\varphi_{12} \geqslant 140^\circ$) relative azimuthal angles. In these regions the calculations including Coulomb interaction provide more adequate results than other ones, though in some cases the Coulomb effect is less pronounced in the data than predicted by theory.
(3) The overall description of the data for configurations with $\varphi_{12} \leqslant 100^\circ$ is good. Even if the experimental points systematically lie above the theories, these differences are comparable to systematic uncertainties, and such a correlated behavior suggests that the source lies in uncertainty of the luminosity.
(4) In configurations with the largest studied polar angles ($\theta_1 = \theta_2 = 13^\circ, 15^\circ$), nearly coplanar ($\phi_{12} = 160^\circ, 180^\circ$), the theoretical predictions deviate very strongly from the data, underestimating them. The differences are significantly larger than the uncertainties of the data.

These observations will be further quantitatively discussed by means of a χ^2/d.o.f. analysis.

A. χ^2 analysis

Quantitative analysis of the description of the cross-section data (σ_{exp}) provided by various calculations (σ_{teor}) is performed in terms of χ^2-like variables. Due to the dominating contribution of systematic uncertainties, the following definition has been applied, which also facilitates direct comparisons with the results from Ref. [25]:

$$\chi^2 = \frac{1}{n_{\text{d.o.f.}}} \sum \frac{(\sigma_{\text{teor}}(\xi) - \sigma_{\text{exp}}(\xi))^2}{(\Delta\sigma_{\text{st}}(\xi) + \Delta\sigma_{\text{sys}}(\xi))^2}, \tag{2}$$

where ξ represents a set of kinematic variables $\xi = (\theta_1, \theta_2, \varphi_{12}, S)$, $\Delta\sigma_{\text{st}}(\xi)$, and $\Delta\sigma_{\text{sys}}(\xi)$ denote statistical and systematic uncertainties, respectively, the summing goes over a certain set of kinematic variables, and $n_{\text{d.o.f.}}$ is a number of data points included in this sum. The quantity defined in this way has no precise statistical meaning, but it still provides a measure of the description provided by different models and allows comparison of possible deviations with experimental uncertainties. Directly adding (not squaring) the two contributions to the uncertainty in the denominator of the above formula yields the maximum error, but given the dominance of systematic error, this choice has a negligible effect on the result.

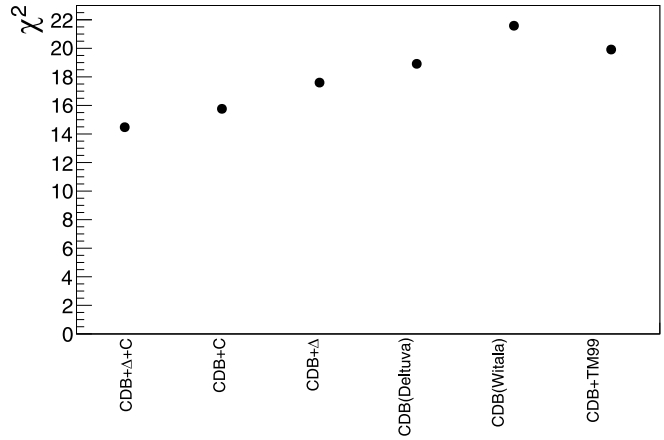

FIG. 7. Quality of description of the differential cross section for the breakup reaction at 190 MeV/nucleon beam energy at forward angles. The global χ^2/d.o.f. (systematic errors included) was obtained as a result of comparing the cross-section data with each of six types of theoretical calculations specified on the axis.

The χ^2/d.o.f. defined above has been calculated globally, individually for the kinematic configurations and, in addition, for the data sorted according to combination of polar angles θ_1, θ_2 or a relative azimuthal angle φ_{12} of the two protons. The global analysis (see Fig. 7) indicates that the quality of the description of the data is worse than for the data at 170 MeV/nucleon energy, where analogously defined χ^2/d.o.f. values covered the range between 3 and 7 [25]. Current values obtained at the beam energy of 190 MeV/nucleon are roughly 3 times higher, which is surprising given the small difference in beam energies and the same angular range in the laboratory system and thus a very similar phase space. Global analysis indicates an improvement in description due to the inclusion of Coulomb interaction or of 3NF (TM99 force or explicit Δ isobar approach), with the best result achieved when both contributions are included. However, the aforementioned effects are small compared to the global imperfection of the description.

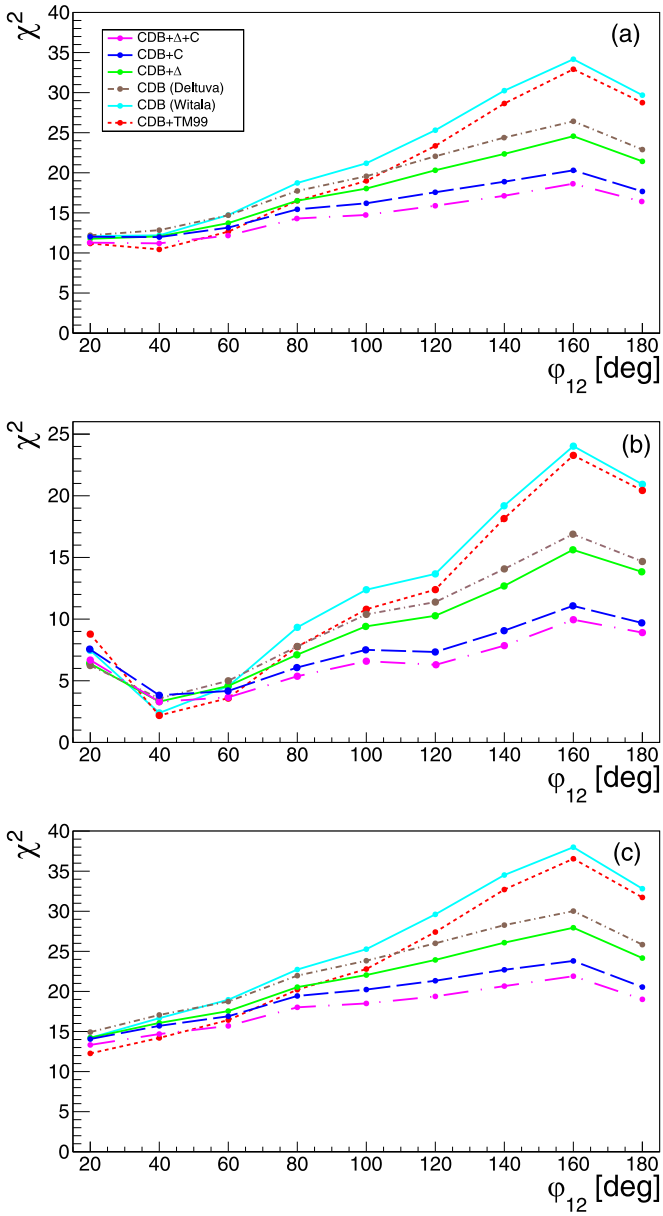

FIG. 8. The χ^2/d.o.f. calculated for set of data characterized with given relative azimuthal angle ϕ_{12}: (a) whole S distrubutions were taken into account; (b) only central parts of S distrubutions were taken into account; (c) only tails of S distrubutions were taken into account.

In order to ascertain whether the deterioration of the description occurs in the entire phase space studied in the experiment, and to look for areas sensitive to individual contributors to the dynamics, the quality of description was studied in a function of kinematic variables. Dependence of χ^2/d.o.f. on φ_{12} angle was examined first. The analysis [see Fig. 8(a)] clearly indicates the region of dominance of the Coulomb effect at the largest relative azimuthal angles. Surprisingly, the improvement of description related to introducing Coulomb interactions is not so obvious in the region of the lowest ϕ_{12}, close to proton-proton FSI. Calculations predict there strong sensitivity to Coulomb interaction, which lowers cross section, but in certain configurations data lie just between calculations with and without Coulomb interaction (see, for example, a configuration of $\theta_1 = 5^\circ$, $\theta_2 = 5^\circ$, $\varphi_{12} = 20^\circ$ in Fig. 11), resulting in similar χ^2/d.o.f. for both cases.

Already at the beam energy of 170 MeV/nucleon, a significant difference in the shapes (widths) of cross-section distributions was observed: Experimental S distributions were wider than theoretical ones [25]. This effect might be partially attributed to relativistic effects in kinematics, but persists even for relativistic calculations. In the dataset presented here, experimental distributions shown in Fig. 6 are characterized by from 12 to 19% larger RMS than the theoretical ones (calculated for the same range of S). Variations of widths between various theoretical calculations are between 4 and 6%, depending on configurations, while impact of averaging on their RMS is of about 1%. The impact of the instrumental resolution was studied by the width of the event distribution around the kinematics (see example in Fig. 3) and the corresponding RMS was found to range between 3.0 and 3.5 MeV. The discussed above differences are much larger. For configuration $\theta_1 = 5^\circ$, $\theta_2 = 5^\circ$, $\varphi_{12} = 60^\circ$ the maximal RMS for theories equals to 24.1 MeV and the RMS for the experimental distribution equals to 27.7 MeV. Thus, convoluting the theoretical value with the instrumental resolution do not influence the result.

To examine impact of the difference of shapes on the quality of the data description, the above presented analysis of χ^2/d.o.f. in a function of φ_{12} was repeated separately for two data subsets: data points lying in the central part of each kinematics (maximum of the cross-section distribution) and data belonging to the tails of the distributions, see respectively Figs. 8(b) and 8(c). The general trends are similar, but the values differ considerably (note the differences in the scale of the vertical axes). In the case of CDB+Δ+C calculations, χ^2/d.o.f. values are 2 or 3 times lower for peaks than for tails, in the former case they range from 4 to 9. Also the contribution of tails to χ^2/d.o.f. is rather uniform, see Fig. 8(c), while for peaks [Fig. 8(b)], the quality of description in particular regions is more diverse and model dependent. The data are generally well described by all the models for φ_{12} of 40° and 60°, where the sensitivity to the interaction dynamics included in the calculations is low. The Coulomb interaction has a large impact at high φ_{12}. Adding 3NF slightly improves the description.

In summary, this analysis indicates that a large part of the discrepancy at the studied energy stems from the difference in the widths of the experimental and theoretical distributions. Discrepancies in the peak region accumulate at high φ_{12}.

The analysis of data sorted with respect to polar angles θ_1, θ_2 (Fig. 9) was carried out in two variables: difference $\theta_2 - \theta_1$ reflecting "asymmetry" of the configuration (individual panels in Fig. 9, look at the different scales on the horizontal axis between them) and an average of the polar angles $(\theta_1 + \theta_2)/2$. Clearly, the Coulomb force dominates in the FSI region, characterized by the lowest difference of polar angles and the lowest average polar angles, between 5° and 7°. Moreover, description of the data improves with rising

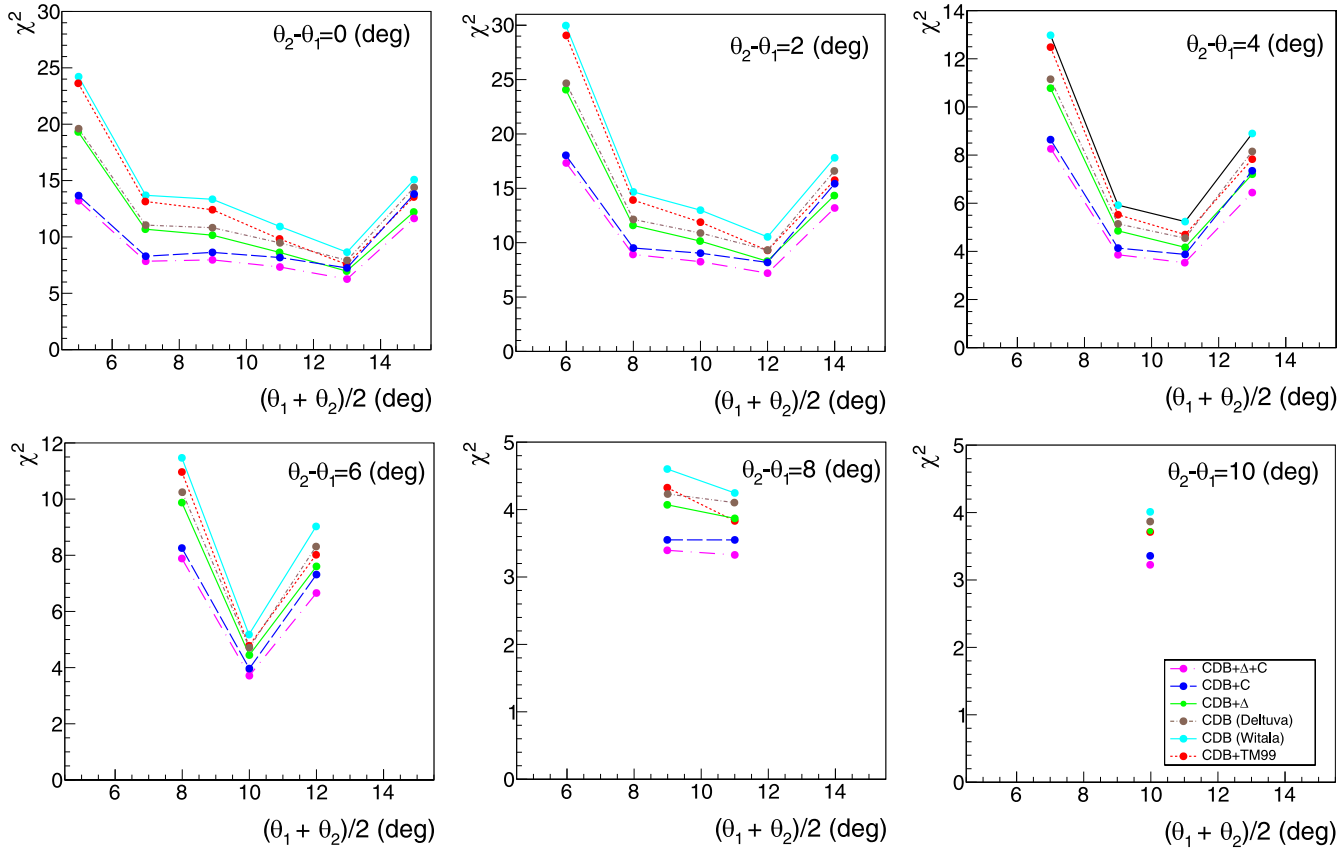

FIG. 9. The χ^2/d.o.f. calculated for each set of data characterized with the given combination of proton polar angles. The results are ordered according to difference of polar angles $\theta_{12} = \theta_1 - \theta_2$; in each panel results for one value of θ_{12} are shown.

asymmetry of polar angles and/or for a medium average of about 10°. The region of certain sensitivity to 3NF can be, in turn, identified at more symmetric configurations (three top panels) with high average $(\theta_1 + \theta_2)/2 \geqslant 13°$, but this effect is tiny.

The maps of χ^2/d.o.f. for individual configurations prepared for four theoretical calculations are shown in Fig. 10. For the purpose of this comparison, a set of theories has been chosen that allows the Coulomb and 3NF effects to be traced both separately and together. For better visibility of effects, the maximum of color z axis was artificially set to 25. In all the maps, one can observe a kind of stepped pattern corresponding to the fact that the configurations more asymmetric in polar angles are better described by the theories. In the case of CDBonn potential alone, it is apparent that for $\varphi_{12} > 100°$ (right hand side of the map) the agreement between data and theory is poor. Only a small change in the picture due to 3NF (CDB+Δ) is observed, as expected from the small size of these predicted effects. On the map corresponding to the CDB+C calculations the improvement of description is clearly visible. Adding both Coulomb interaction and 3NF (CDB+Δ+C) leads to a further small improvement of the description. In the region of large polar and azimuthal angles (top right corner of the map), a lot of room for improvement remains, as was expected from examining particular cross-section distributions in Fig. 6.

Since the same normalization factor was applied to the entire dataset, we conducted a similar analysis using a slightly different approach that separates the normalization factor from the other contributions, which are individual for configurations or data points. The contributions from systematic uncertainties of luminosity were removed from the uncertainties of individual data points, while the normalization factor was varied within the range allowed by these uncertainties. The resulting global chi-squared values for the four cases, taking into account the systematic uncertainty in luminosity and not taking, for nominal normalization and the two extreme cases, are presented in the Table II, and the corresponding maps are included in Appendix B, Fig. 22. For the nominal value [panel (b)], we obtain slightly higher values (due to a reduction in systematic uncertainties), but the effect is minor and does not alter the conclusions. For the minimum luminosity values allowed by our analysis, i.e., 8% lower than the nominal value [panel (d)], there is a drastic deterioration in the quality of the global description and in a large portion of the χ^2/d.o.f. map. For the maximum value (3% higher than nominal [panel (c)]), both the global values and the χ^2/d.o.f. map are very similar to those from the previously described analysis.

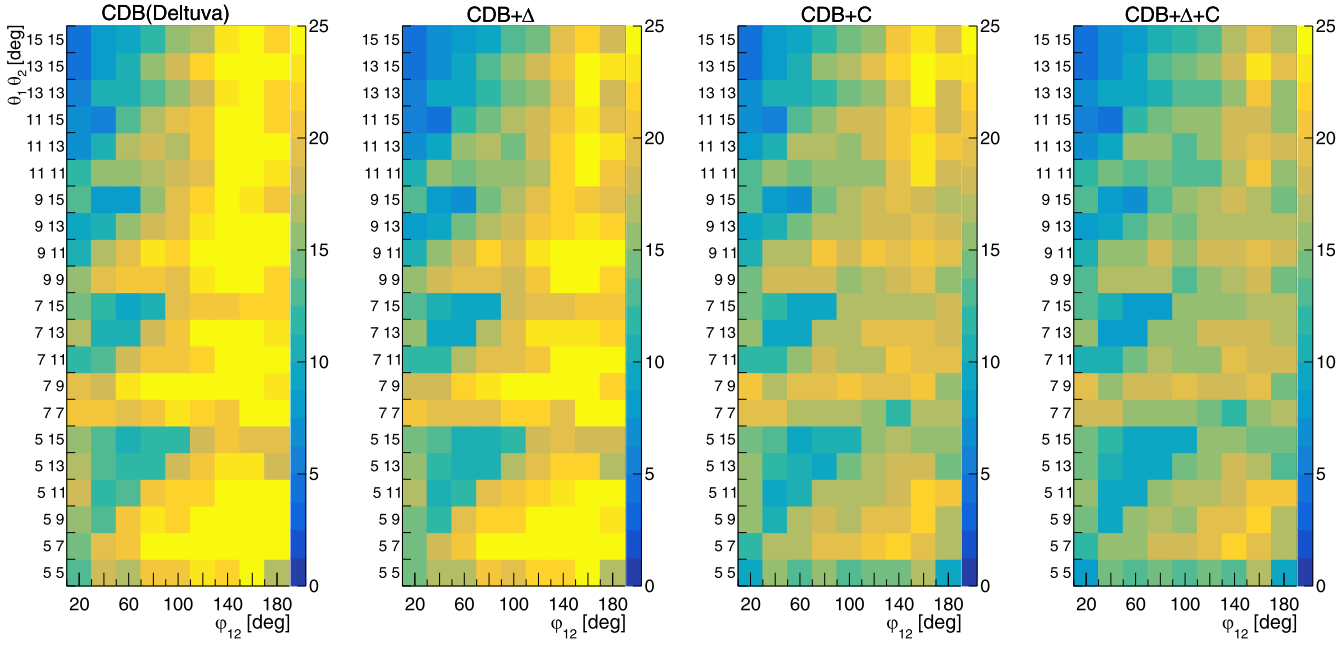

FIG. 10. The χ^2/d.o.f. results obtained for all angular configurations separately, presented as the two-dimensional map for selected theories, specified at the top of panels.

V. SUMMARY

The measurement of differential cross section of the ^{1}H$(d, pp)n$ reaction at three beam energies, 170, 190, and 200 MeV/nucleon, changed in a supercycle mode allowed good control over data consistency and experimental uncertainties, constituting the basis for systematic comparison of the results. In this work, the differential cross section for beam energy 190 MeV/nucleon is presented for 189 configurations characterized with forward proton emission angles in the laboratory system and compared to a set of theoretical calculations. In this region, predicted 3NF effects are small, whereas calculated Coulomb effects are significant, especially at low polar angles of emitted protons. Relativistic calculations were performed for several selected configurations with the CD-Bonn potential alone, showing a significant influence on the cross section compared to the same calculations in the nonrelativistic approach.

Confronting these predictions with the data, we clearly confirm observation of the Coulomb effects, though in some cases calculations including Coulomb interactions underestimate the data. It is not clear whether this can be attributed to relativistic effects or to another missing dynamical effect. Moreover, a general deterioration of the overall data description is observed, as compared to data collected at slightly lower beam energy of 170 MeV/nucleon. It has been shown that this is largely related to the difference in the widths of the theoretical and experimental cross-section S distributions. Apart from that, the description of data in the peaks is quite successful for a majority of configurations, in particular after Coulomb interaction is included, with differences falling within the range of systematic uncertainties.

We have, however, localized a set of kinematical configurations of large disagreements between the experimental data and all the available theoretical calculations. This mainly concerns configurations with polar angles of $\theta_1 = \theta_2 = 13^\circ$ or 15° and coplanar or nearly coplanar geometries ($\varphi_{12} = 160^\circ, 180^\circ$), where the differential cross section is the lowest in the studied phase space. The discrepancies between the data and the theories of a factor of roughly 2 are observed. The latter finding is consistent with that followed from the previously analyzed cross-section data at 170 MeV/nucleon. There, local underestimation of data with theories was observed for exactly the same configurations. Comparisons of these two datasets indicate that the discrepancy increases with beam energy. Calculations performed in the relativistic approach, limited to the CD-Bonn potential, further increase the discrepancy, leaving room for very large effects of the 3NF, well beyond the predictions of current models. This suggests either problem with currently available 3NF's at so high energy or huge relativistic effects in the 3NF's.

Importantly, similar underestimation the data by theoretical predictions was observed in the cross-section data collected at the same center-of-mass energy but in the direct kinematics ^{2}H$(p, pp)n$ [22–24]. There the discrepancies were also observed locally in symmetric configurations with $\varphi_{12} \geqslant 160^\circ$. In spite of these similarities, those configurations corresponded to a different $\theta_{\text{c.m.}}$ region. Also, in the regions of disagreements the predicted relativistic effects were small: Either negligible or shifting the results of calculations slightly towards the data, though far too small to solve the problem. Two independent experiments have therefore observed significant problems with the description of the differential cross

TABLE II. Quality of description of the differential cross section for the breakup reaction at 190 MeV/nucleon beam energy at forward angles. The global χ^2/d.o.f. was obtained as a result of comparing the cross-section data with each of six types of theoretical calculations (see Fig. 7). The subsequent columns in the table [marked as (a), (b), (c), and (d)] show the χ^2/d.o.f. values for the four cases, taking into account the systematic uncertainty in luminosity (a) and without this contribution (b)–(d), for nominal normalization (b) and the two extreme normalization factors, corresponding to maximum (c) and minimum (d) luminosity. The corresponding χ^2/d.o.f. maps for CDB +Δ+ C theoretical calculations can be found in Fig. 22, in Appendix B.

	χ^2/d.o.f.			
Theory	(a)	(b)	(c)	(d)
CDB+Δ+C	14.5	16.2	14.8	20.6
CDB+C	15.8	17.7	16.2	22.1
CDB+Δ	17.6	19.8	18.3	24.2
CDB(Deltuva)	18.9	21.2	19.7	25.7
CDB(Witala)	21.6	24.3	22.9	28.5
CDB+TM99	19.6	22.5	21.2	26.6

section at this energy in two different kinematic regions, characterized by different relativistic effects in the *NN* interaction.

Systematic studies of the deuteron breakup in collision with proton at relatively high energies are important for testing current approaches to describe nuclear interactions. The differential cross section exhibits surprising sensitivity to missing elements of the dynamics, as well as in the regions where current 3NF models do not predict any spectacular effects. Since relativistic calculations based on pure *NN* interaction show the effect opposite to the one needed for the correct data description, an approach that takes into account relativistic effects together with a full complexity of interaction potential, including 3NF, would be of great interest.

ACKNOWLEDGMENTS

This work was partly supported by the National Science Centre, Poland, under Grant No. IMPRESS-U 2024/06/Y/ST2/00135 and by the Excellence Initiative–Research University Program at the Jagiellonian University in Kraków. The numerical calculations were partly performed on the supercomputers of the JSC, Jülich, Germany. We thank the COSY crew for their work and the excellent conditions during the beam time.

DATA AVAILABILITY

The data that support the findings of this article are openly available [47].

APPENDIX A

Appendix A contains all the differential cross-section distributions for the ^{1}H$(d, pp)n$ breakup reaction at the beam energy of 190 MeV/nucleon obtained in the analysis described in this paper (Figs. 11–21). Each set presents nine configurations corresponding to individual azimuthal angles φ_{12} from 20° to 180° and one combination of θ_1 and θ_2 specified in the figure. Since the 3NF effects are generally small and the results weakly depend on the model used, for clarity only calculations with one 2N potential (CD-Bonn) and one 3NF model (explicit treatment of Δ isobar) are shown.

APPENDIX B

Appendix B presents χ^2/d.o.f. values obtained for all the studied angular configurations of the breakup reaction at 190 MeV/nucleon for calculations with the CDB+Δ+C potential (Fig. 22). Similarly to Fig. 10, they are presented as the two-dimensional maps and were obtained using two approaches to treat the systematic uncertainties combined with three cross-section normalization factors. For the reference, the far-right panel of Fig. 10 is repeated, which corresponds to the standard normalization factor used in this analysis ("nominal" luminosity) and taking into account the contribution of systematic uncertainty of luminosity to the total systematic uncertainty. The other three maps [panels (b)–(d)] were obtained without this contribution to the systematic uncertainty, and with three normalization factors related to the nominal luminosity and the two extreme cases allowed by the systematic uncertainties (see also the discussion in Sec. IV and Table II).

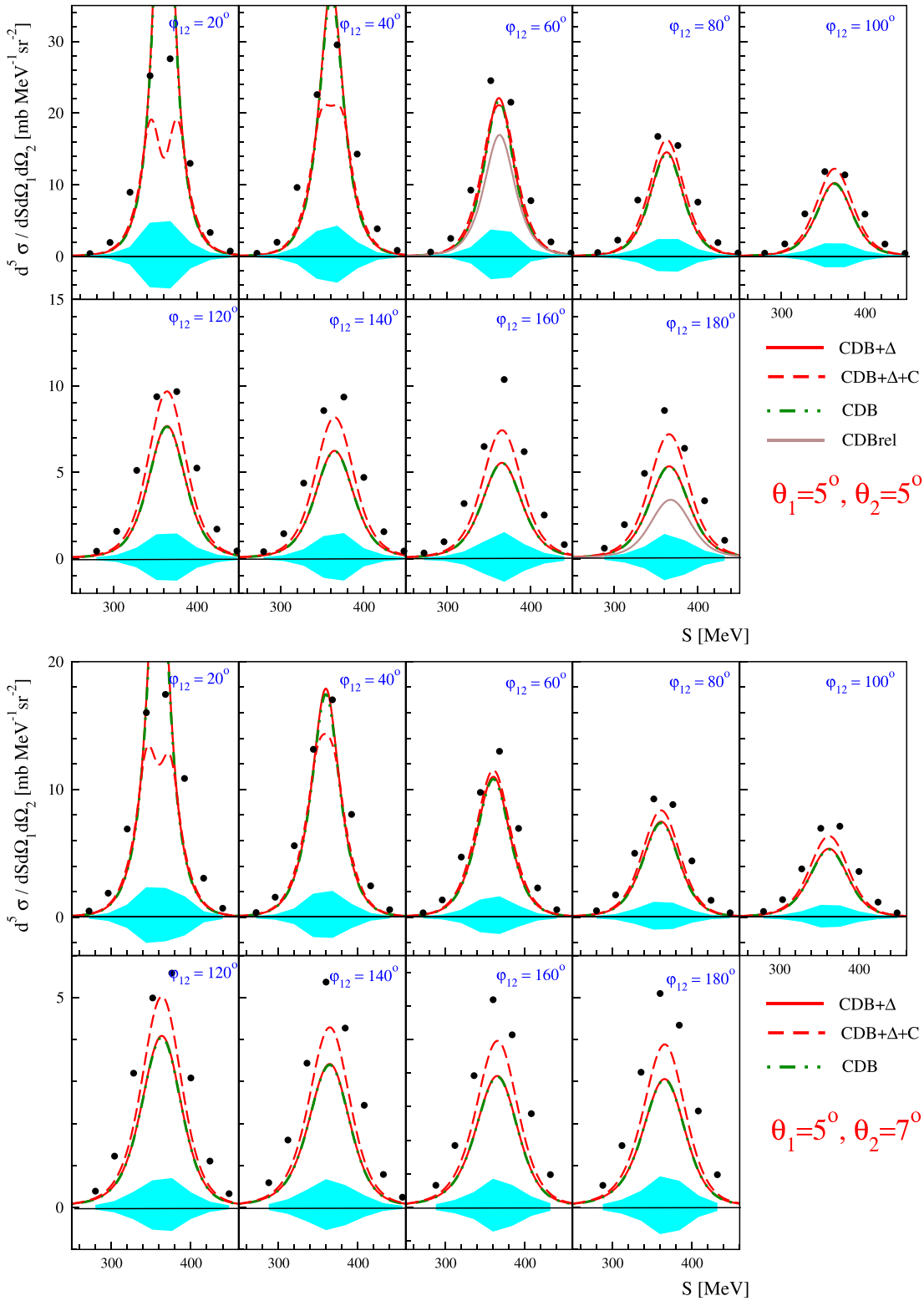

FIG. 11. Differential cross section of ^{1}H(d, pp)n breakup reaction at beam energy of 190 MeV/nucleon shown in function of S variable. The presented data belong to nine kinematic configurations characterized with the same combinations of proton polar angles ($\theta_1 = 5^\circ$, $\theta_2 = 5^\circ$ in the top part and $\theta_1 = 5^\circ$, $\theta_2 = 7^\circ$ in the bottom part) and various relative azimuthal angles of the two protons, indicated in the individual panels. Statistical errors are smaller than the size of the points. Systematic uncertainties are represented by bands. Theoretical calculations are shown as lines specified in the legend.

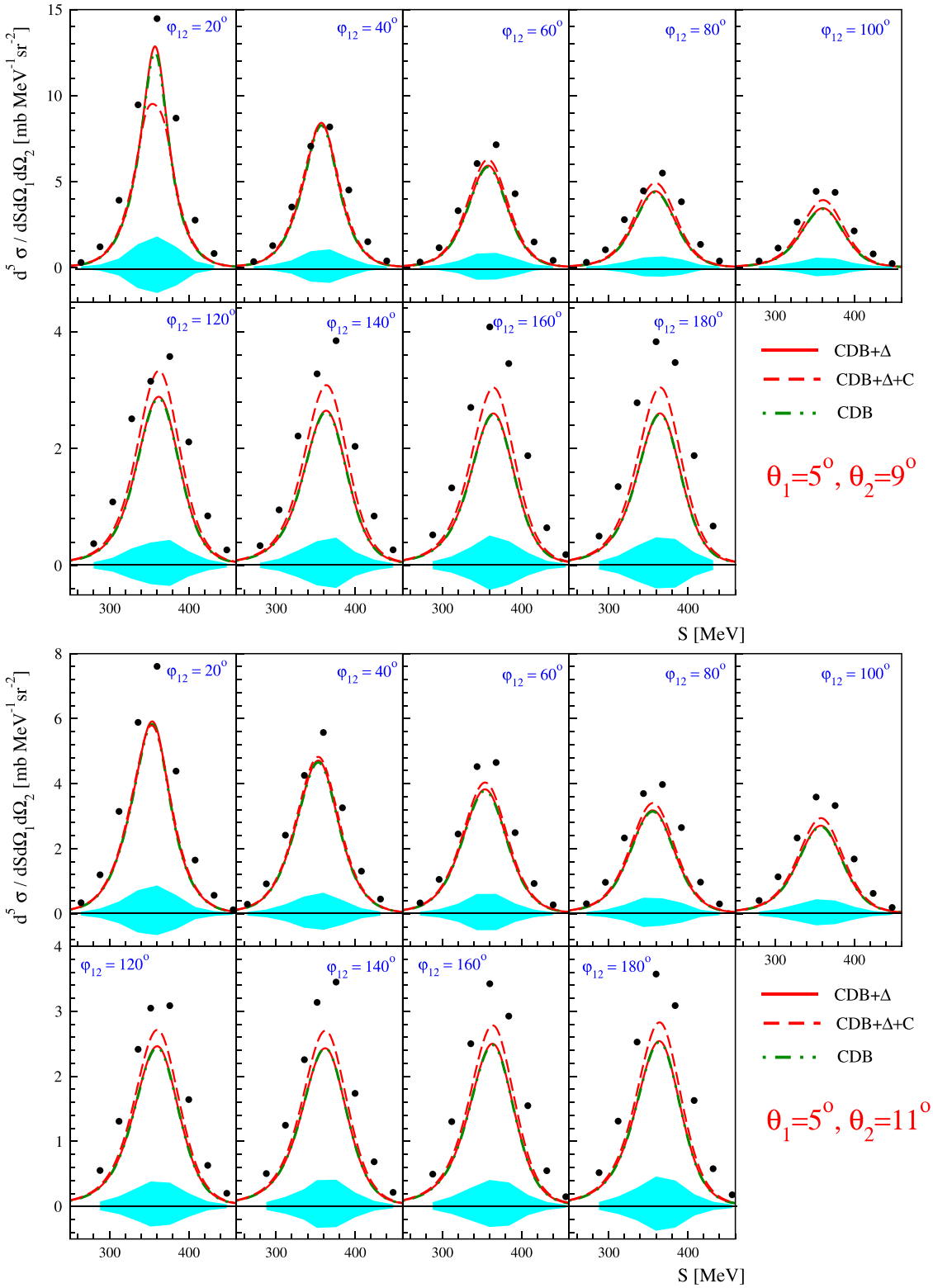

FIG. 12. The same as Fig. 11 but for kinematic configurations with the proton polar angles $\theta_1 = 5^\circ$, $\theta_2 = 9^\circ$ and $\theta_1 = 5^\circ$, $\theta_2 = 11^\circ$.

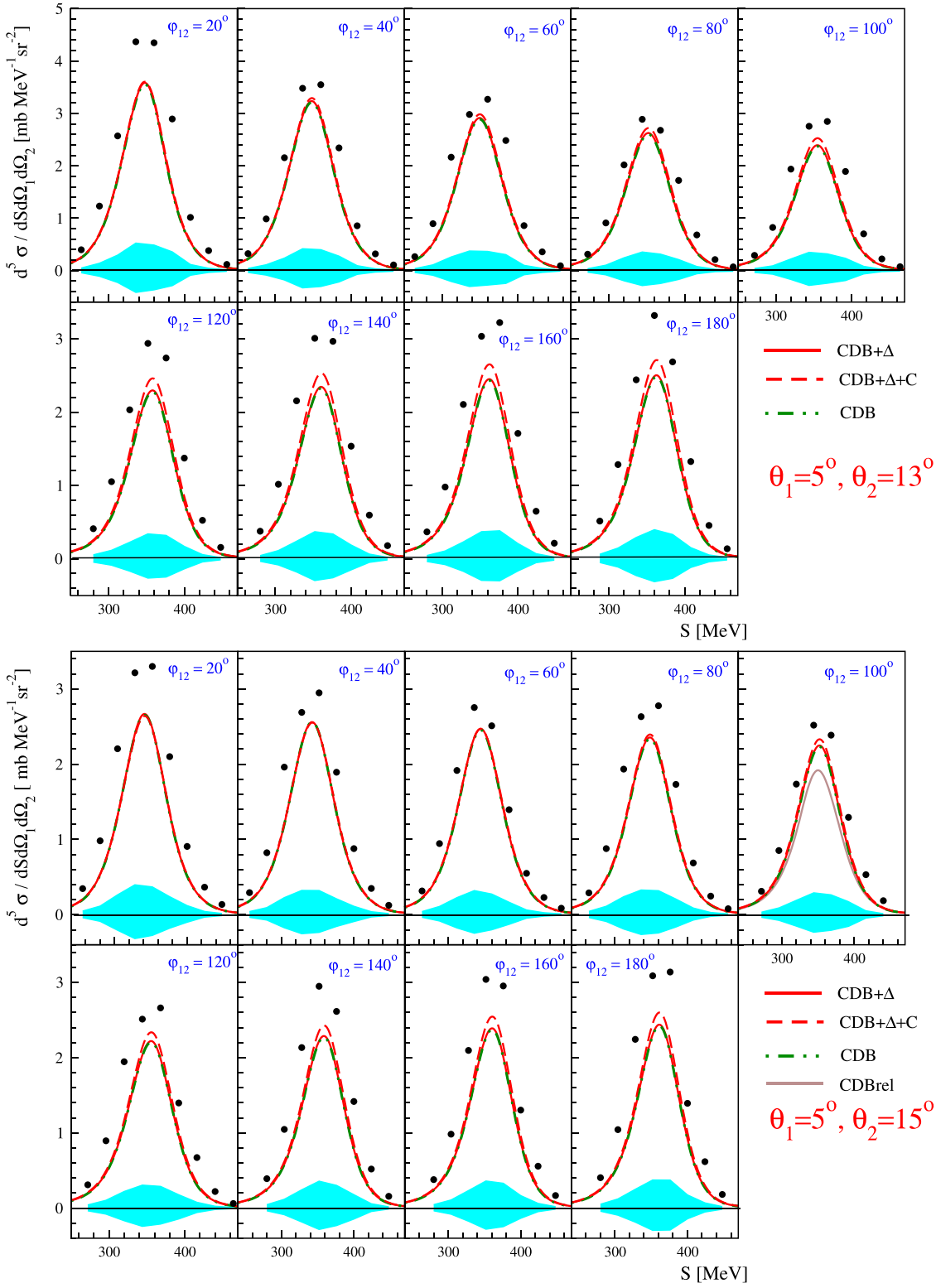

FIG. 13. The same as Fig. 11 but for kinematic configurations with the proton polar angles $\theta_1 = 5°$, $\theta_2 = 13°$ and $\theta_1 = 5°$, $\theta_2 = 15°$.

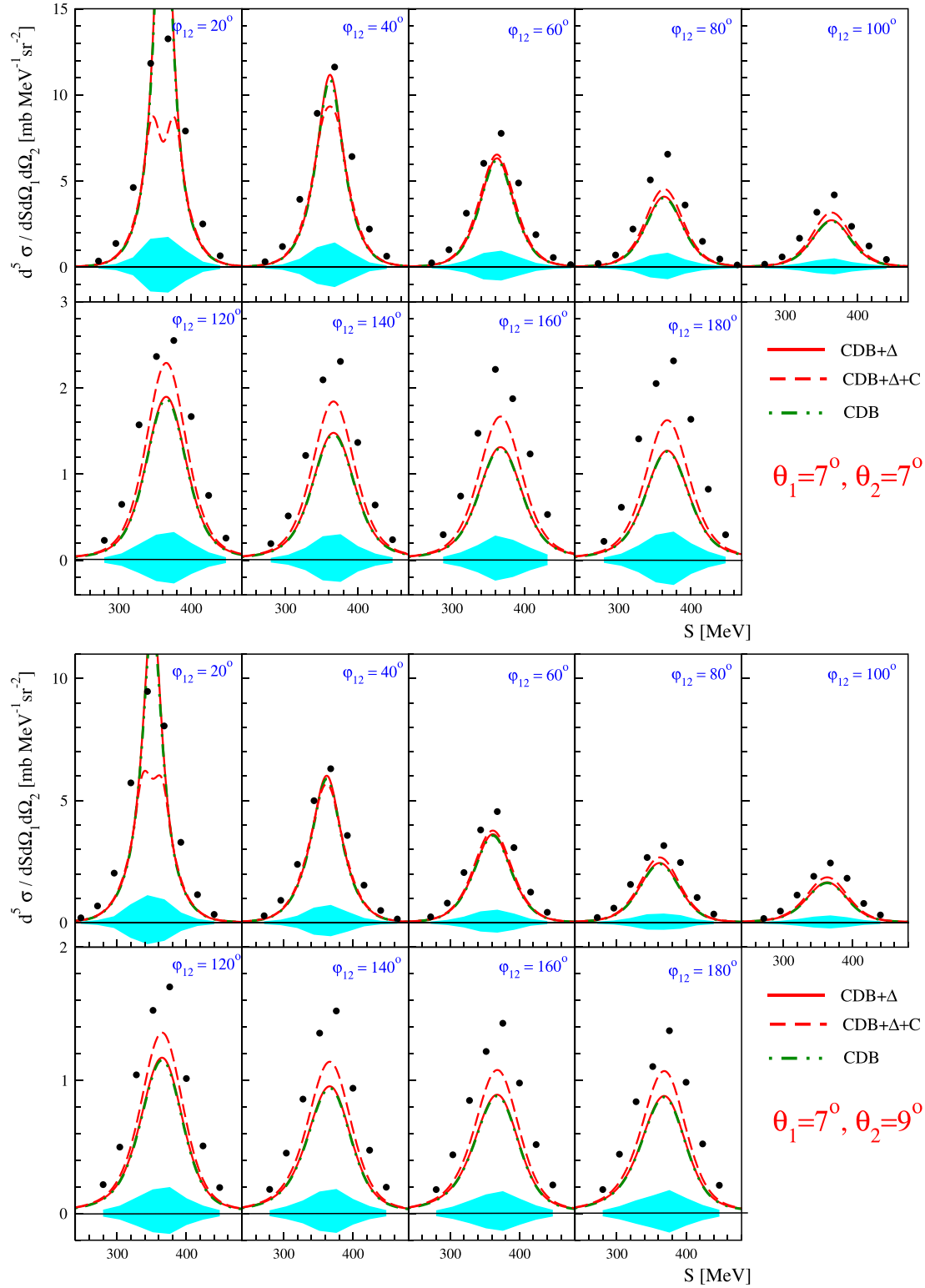

FIG. 14. The same as Fig. 11 but for kinematic configurations with the proton polar angles $\theta_1 = 7^\circ$, $\theta_2 = 7^\circ$ and $\theta_1 = 7^\circ$, $\theta_2 = 9^\circ$.

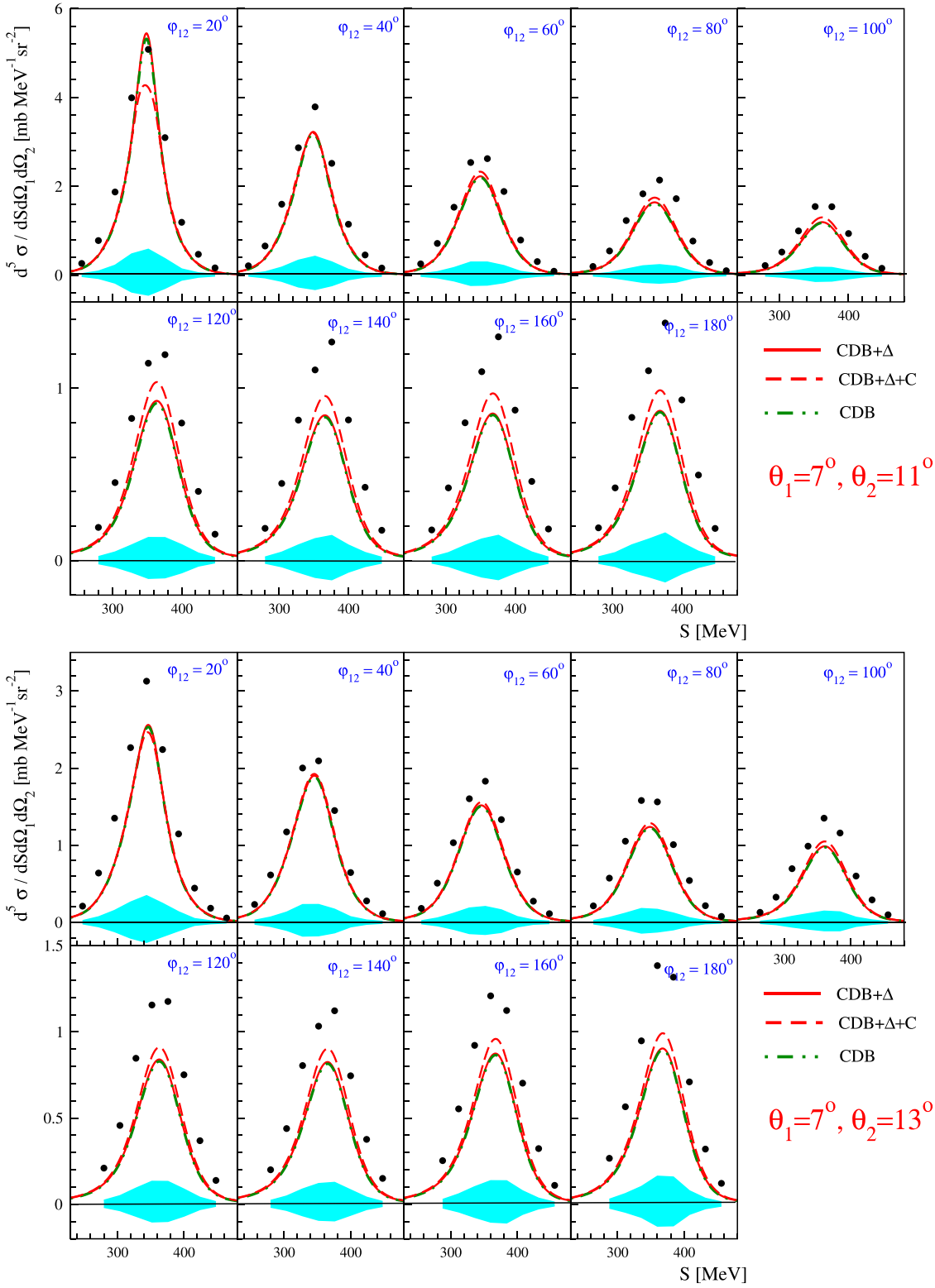

FIG. 15. The same as Fig. 11 but for kinematic configurations with the proton polar angles $\theta_1 = 7^\circ$, $\theta_2 = 11^\circ$ and $\theta_1 = 7^\circ$, $\theta_2 = 13^\circ$.

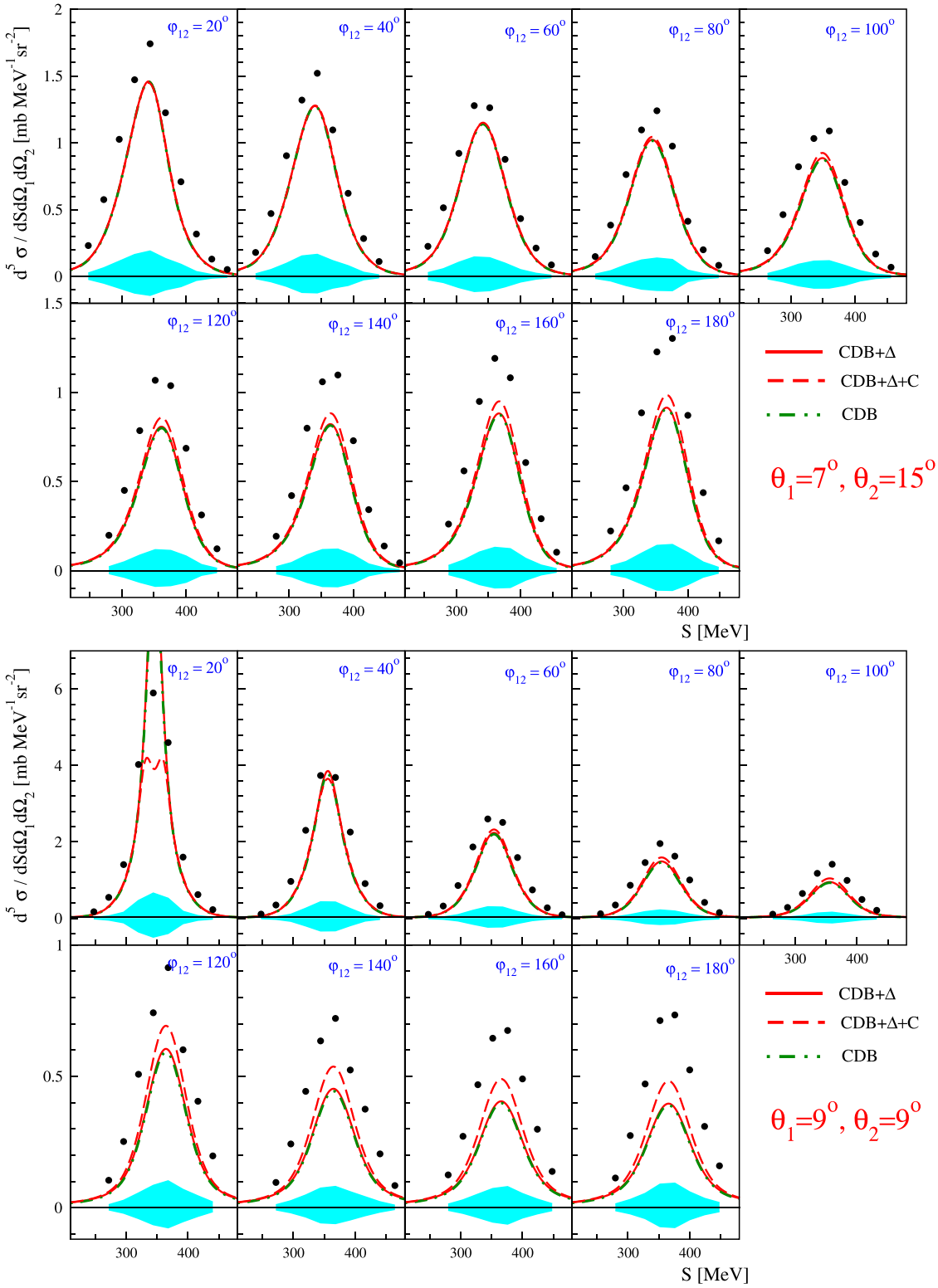

FIG. 16. The same as Fig. 11 but for kinematic configurations with the proton polar angles $\theta_1 = 7^\circ$, $\theta_2 = 15^\circ$ and $\theta_1 = 9^\circ$, $\theta_2 = 9^\circ$.

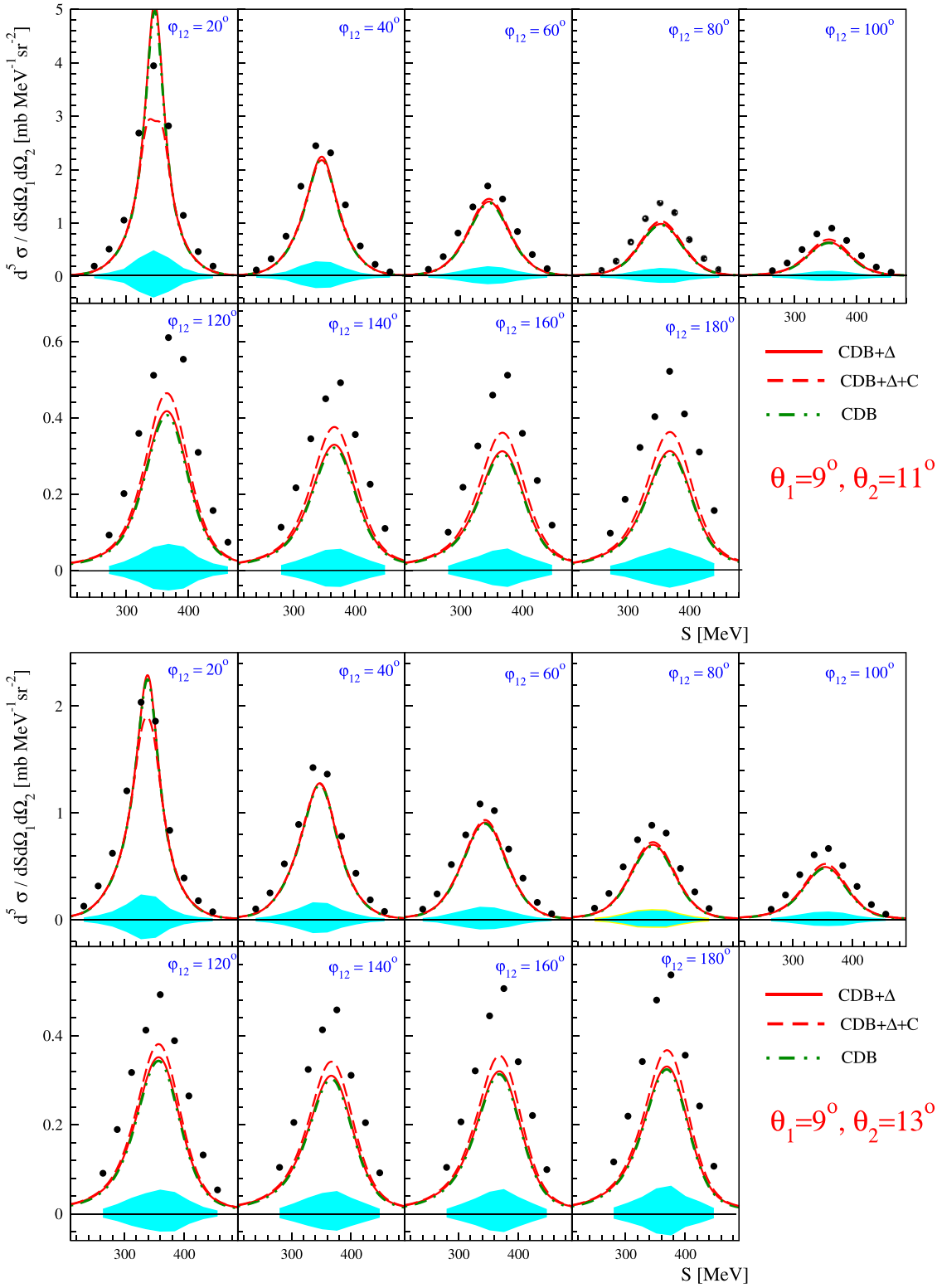

FIG. 17. The same as Fig. 11 but for kinematic configurations with the proton polar angles $\theta_1 = 9°$, $\theta_2 = 11°$ and $\theta_1 = 9°$, $\theta_2 = 13°$.

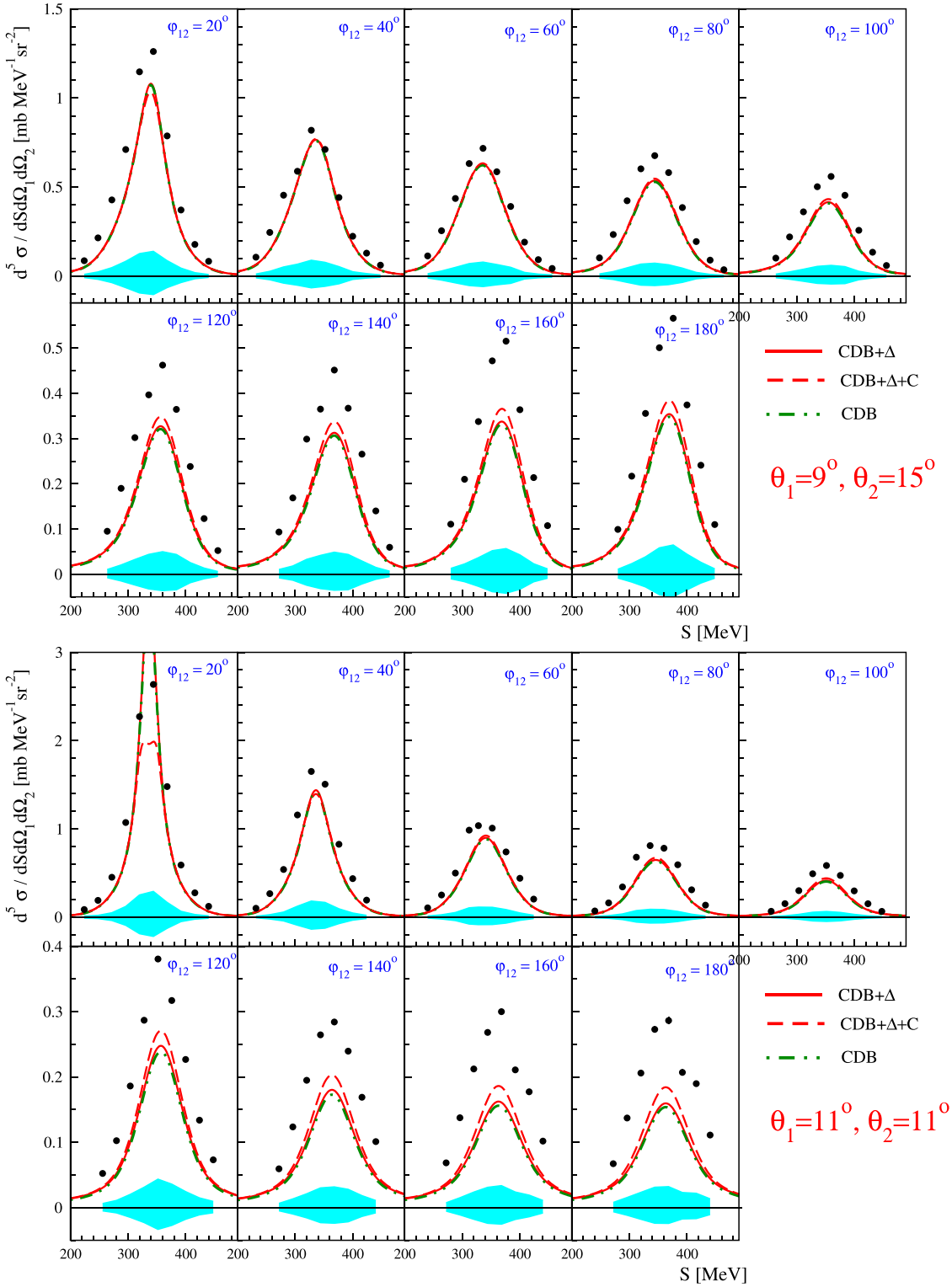

FIG. 18. The same as Fig. 11 but for kinematic configurations with the proton polar angles $\theta_1 = 9^\circ$, $\theta_2 = 15^\circ$ and $\theta_1 = 11^\circ$, $\theta_2 = 11^\circ$.

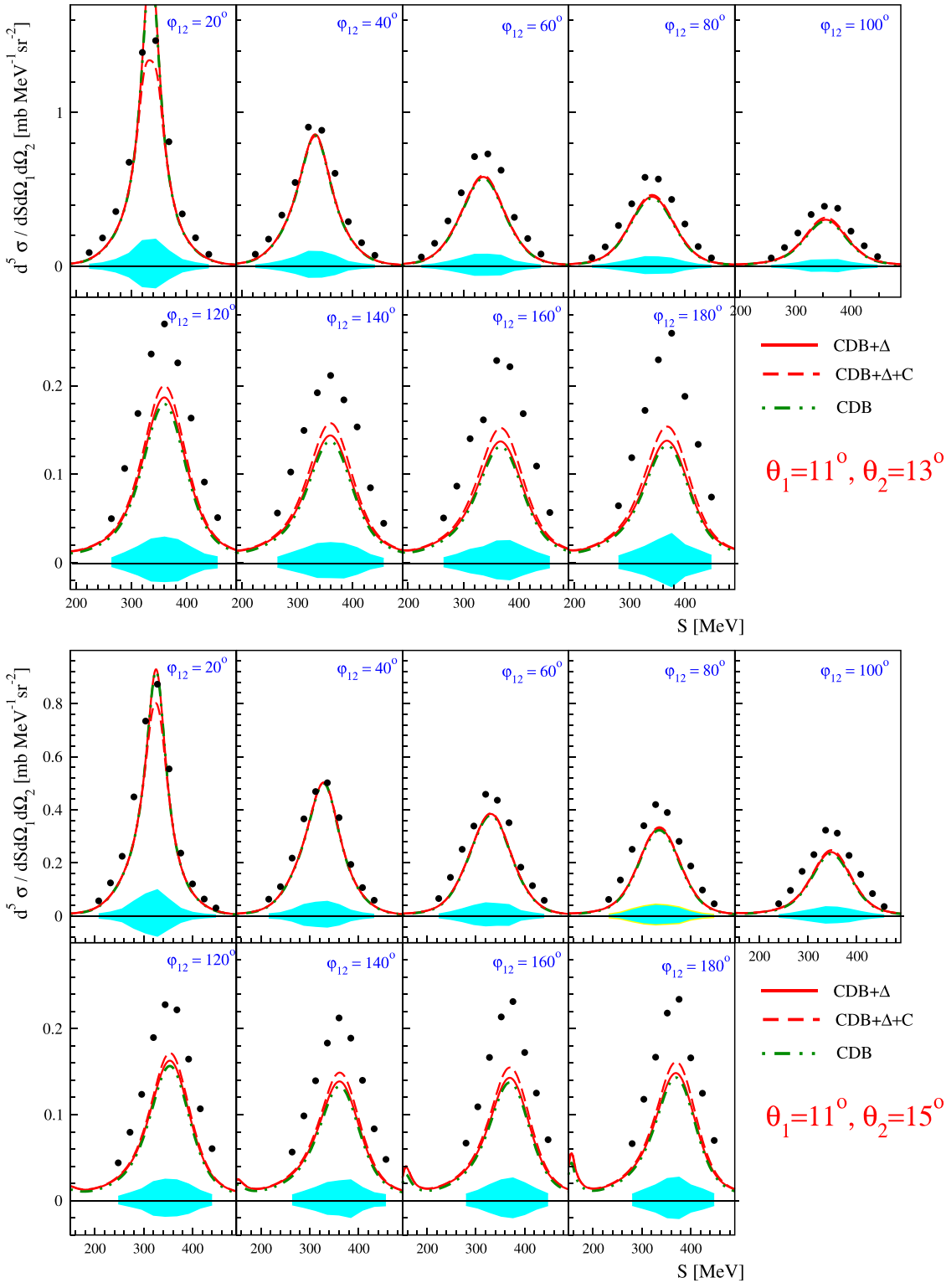

FIG. 19. The same as Fig. 11 but for kinematic configurations with the proton polar angles $\theta_1 = 11^\circ$, $\theta_2 = 13^\circ$ and $\theta_1 = 11^\circ$, $\theta_2 = 15^\circ$.

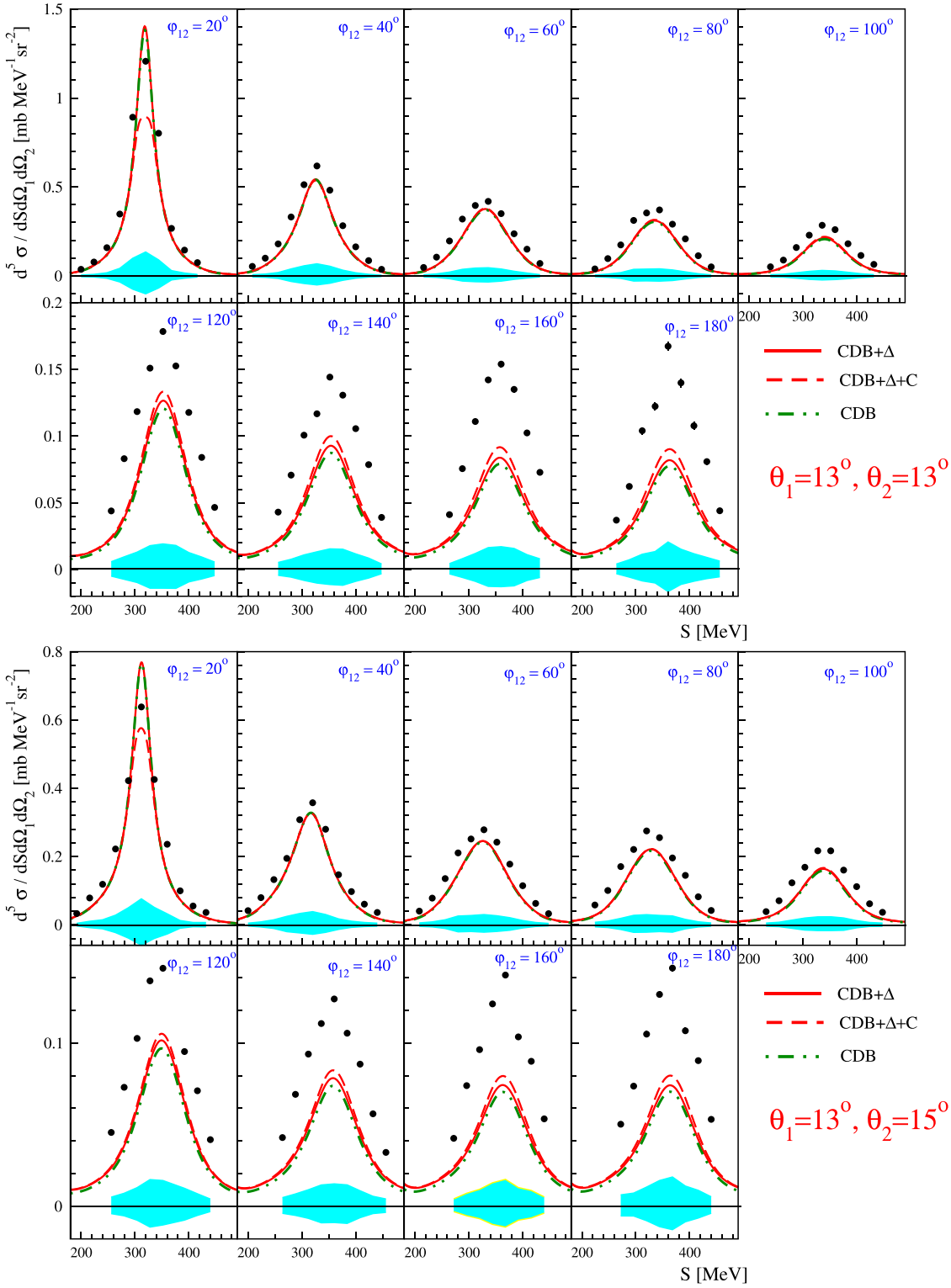

FIG. 20. The same as Fig. 11 but for kinematic configurations with the proton polar angles $\theta_1 = 13^\circ$, $\theta_2 = 13^\circ$ and $\theta_1 = 13^\circ$, $\theta_2 = 15^\circ$.

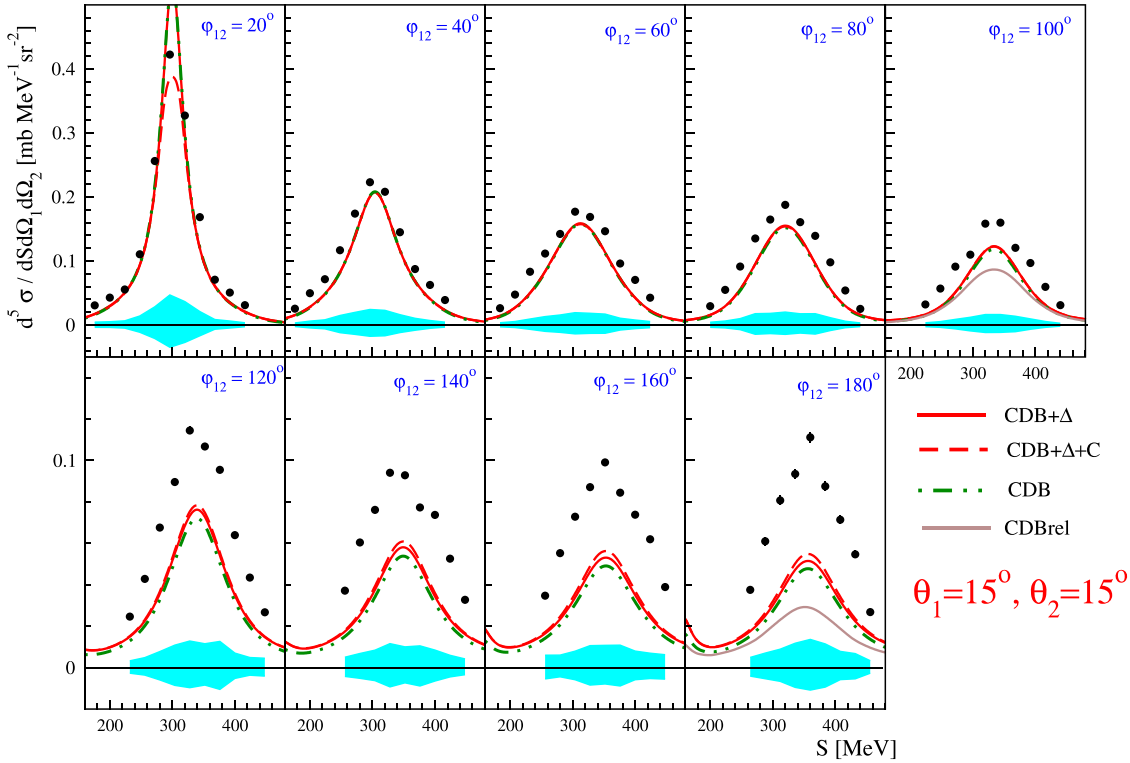

FIG. 21. The same as Fig. 11 but for kinematic configurations with proton polar angles $\theta_1 = 15^\circ$, $\theta_2 = 15^\circ$.

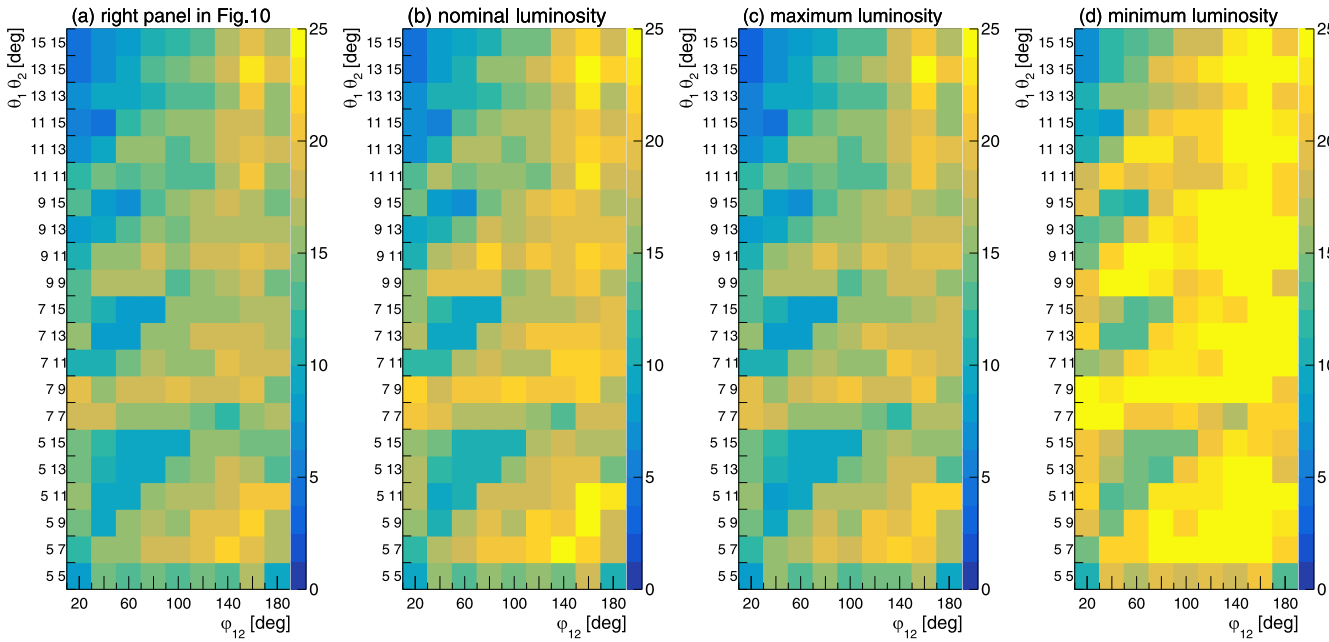

FIG. 22. The χ^2/d.o.f. results obtained for all analyzed angular configurations separately, presented as the two-dimensional maps for CDB+Δ+C theoretical calculations. Panel (a) is a replication of the result from Fig. 10. Panels (b)–(d) correspond to analysis with the systematic uncertainty in luminosity not included into calculations of χ^2/d.o.f. carried out using three different normalization factors: the nominal value (b), the maximum permitted luminosity value in terms of systematic uncertainty (c), and the minimum permitted luminosity value in terms of systematic uncertainty (d). For more details see the text.

[1] S. A. Coon and H. K. Han, Reworking the Tucson-Melbourne three-nucleon potential, Few-Body Syst. **30**, 131 (2001).

[2] B. S. Pudliner, V. R. Pandharipande, J. Carlson, S. C. Pieper, and R. B. Wiringa, Quantum Monte Carlo calculations of nuclei with $A < 7$, Phys. Rev. C **56**, 1720 (1997).

[3] S. C. Pieper, V. R. Pandharipande, R. B. Wiringa, and J. Carlson, Realistic models of pion-exchange three-nucleon interactions, Phys. Rev. C **64**, 014001 (2001).

[4] E. Epelbaum, H.-W. Hammer, and U.-G. Meißner, Modern theory of nuclear forces, Rev. Mod. Phys. **81**, 1773 (2009).

[5] R. Machleidt and F. Sammarruca, Chiral EFT based nuclear forces: Achievements and challenges, Phys. Scr. **91**, 083007 (2016).

[6] J. Carlson, S. Gandolfi, F. Pederiva, S. C. Pieper, R. Schiavilla, K. E. Schmidt, and R. B. Wiringa, Quantum Monte Carlo methods for nuclear physics, Rev. Mod. Phys. **87**, 1067 (2015).

[7] M. Piarulli, A. Baroni, L. Girlanda, A. Kievsky, A. Lovato, E. Lusk, L. E. Marcucci, S. C. Pieper, R. Schiavilla, M. Viviani, and R. B. Wiringa, Light-nuclei spectra from chiral dynamics, Phys. Rev. Lett. **120**, 052503 (2018).

[8] P. Maris, R. Roth, E. Epelbaum, R. J. Furnstahl, J. Golak, K. Hebeler, T. Hüther, H. Kamada, H. Krebs, H. Le, U.-G. Meißner, J. A. Melendez, A. Nogga, P. Reinert, R. Skibiński, J. P. Vary, H. Witała, and T. Wolfgruber, Nuclear properties with semilocal momentum-space regularized chiral interactions beyond N^2LO, Phys. Rev. C **106**, 064002 (2022).

[9] H. Witała, W. Glöckle, D. Hüber, J. Golak, and H. Kamada, Cross section minima in elastic *Nd* scattering: Possible evidence for three-nucleon force effects, Phys. Rev. Lett. **81**, 1183 (1998).

[10] K. Hatanaka, Y. Shimizu, D. Hirooka, J. Kamiya, Y. Kitamura, Y. Maeda, T. Noro, E. Obayashi, K. Sagara, T. Saito, H. Sakai, Y. Sakemi, K. Sekiguchi, A. Tamii, T. Wakasa, T. Yagita, K. Yako, H. P. Yoshida, V. P. Ladygin, H. Kamada, *et al.*, Cross section and complete set of proton spin observables in $p \to d$ elastic scattering at 250 MeV, Phys. Rev. C **66**, 044002 (2002).

[11] P. Mermod, J. Blomgren, B. Bergenwall, A. Hildebrand, C. Johansson, J. Klug, L. Nilsson, N. Olsson, M. Österlund, S. Pomp, U. Tippawan, O. Jonsson, A. Prokofiev, P.-U. Renberg, P. Nadel-Turonski, Y. Maeda, H. Sakai, and A. Tamii, Search for three-body force effects in neutron–deuteron scattering at 95 MeV, Phys. Lett. B **597**, 243 (2004).

[12] S. Kistryn, E. Stephan, A. Biegun, K. Bodek, A. Deltuva, E. Epelbaum, K. Ermisch, W. Glöckle, J. Golak, N. Kalantar-Nayestanaki, H. Kamada, M. Kiš, B. Kłos, A. Kozela, J. Kuroś-Żołnierczuk, M. Mahjour-Shafiei, U.-G. Meißner, A. Micherdzińska, A. Nogga, P. U. Sauer, *et al.*, Systematic study of three-nucleon force effects in the cross section of the deuteron-proton breakup at 130 MeV, Phys. Rev. C **72**, 044006 (2005).

[13] S. Kistryn and E. Stephan, Deuteron–proton breakup at medium energies, J. Phys. G: Nucl. Part. Phys. **40**, 063101 (2013).

[14] S. Kistryn, E. Stephan, B. Kłos, A. Biegun, K. Bodek, I. Ciepał, A. Deltuva, A.C. Fonseca, N. Kalantar-Nayestanaki, M. Kiš, A. Kozela, M. Mahjour-Shafiei, A. Micherdzińska, P.U. Sauer, R. Sworst, J. Zejma, and W. Zipper, Evidence of the Coulomb-force effects in the cross-sections of the deuteron–proton breakup at 130 MeV, Phys. Lett. B **641**, 23 (2006).

[15] I. Ciepał, B. Kłos, S. Kistryn, E. Stephan, A. Biegun, K. Bodek, A. Deltuva, E. Epelbaum, M. Eslami-Kalantari, A. C. Fonseca, J. Golak, N. Kalantar-Nayestanaki, H. Kamada, G. Khatri, D. Kirillov, D. Kirillov, S. Kliczewski, A. Kozela, M. Kravcikova, H. Machner, *et al.*, Investigation of the deuteron breakup on proton target in the forward angular region at 130 MeV, Few-Body Syst. **56**, 665 (2015).

[16] I. Skwira-Chalot, N. Kalantar-Nayestanaki, S. Kistryn, A. Kozela, and E. Stephan, Dynamics of three-nucleon systems at 100 MeV, Few-Body Syst. **65**, 24 (2024).

[17] A. Deltuva, A. C. Fonseca, and P. U. Sauer, Momentum-space description of three-nucleon breakup reactions including the Coulomb interaction, Phys. Rev. C **72**, 054004 (2005).

[18] A. Deltuva, A. C. Fonseca, and P. U. Sauer, New calculation schemes for proton-deuteron scattering including the Coulomb interaction, Phys. Rev. C **73**, 057001 (2006).

[19] A. Deltuva, Momentum-space calculation of proton-deuteron scattering including Coulomb and irreducible three-nucleon forces, Phys. Rev. C **80**, 064002 (2009).

[20] H. Witała, J. Golak, R. Skibiński, W. Glöckle, W. N. Polyzou, and H. Kamada, Relativistic effects in neutron–deuteron elastic scattering and breakup, Few-Body Syst. **49**, 61 (2011).

[21] R. Skibiński, H. Witała, and J. Golak, Relativistic effects in exclusive neutron-deuteron breakup, Eur. Phys. J. A **30**, 369 (2006).

[22] H. Mardanpour, Investigation of nuclear forces in d+p elastic and p+d break-up reactions at intermediate energies, Ph.D. thesis, RUG, 2008.

[23] H. Mardanpour, H. R. Amir-Ahmadi, R. Benard, A. Biegun, M. Eslami-Kalantari, N. Kalantar-Nayestanaki, M. Kiš, S. Kistryn, A. Kozela, H. Kuboki, Y. Maeda, M. Mahjour-Shafiei, J. G. Messchendorp, K. Miki, S. Noji, A. Ramazani-Moghaddam-Arani, H. Sakai, M. Sasano, K. Sekiguchi, E. Stephan, *et al.*, A systematic study of 3NF effects in p + d break-up with BINA at 190 MeV, Few-Body Syst. **44**, 49 (2008).

[24] H. Tavakoli-Zaniani, M. Eslami-Kalantari, H. R. Amir-Ahmadi, M. T. Bayat, A. Deltuva, J. Golak, N. Kalantar-Nayestanaki, S. Kistryn, A. Kozela, H. Mardanpour, J. G. Messchendorp, M. Mohammadi-Dadkan, A. Ramazani-Moghaddam-Arani, R. Ramazani-Sharifabadi, R. Skibiński, E. Stephan, and H. Witała, A comprehensive analysis of differential cross sections and analyzing powers in the proton–deuteron break-up channel at 135 MeV, Eur. Phys. J. A **57**, 58 (2021).

[25] P. Adlarson, W. Augustyniak, W. Bardan, M. Bashkanov, F. S. Bergmann, M. Berłowski, A. Bondar, M. Büscher, H. Calén, I. Ciepał, H. Clement, E. Czerwiński, K. Demmich, R. Engels, A. Erven, W. Erven, W. Eyrich, P. Fedorets, K. Föhl, K. Fransson, *et al.*, Three-nucleon dynamics in *dp* breakup collisions using the WASA detector at COSY-Jülich, Phys. Rev. C **101**, 044001 (2020).

[26] C. Bargholtz, M. Bashkanov, M. Berłowski, A. Bondar, D. Bogoslawsky, W. Brodowski, J. Brudvik, H. Calén, F. Capellaro, A. Chilingarov, H. Clement, J. Comfort, L. Demirörs, C. Ekström, K. Fransson, C.-J. Fridén, L. Gerén, M. Gornov, V. Grebenev, J. Greiff, *et al.*, The WASA detector facility at CELSIUS, Nucl. Instrum. Methods Phys. Res. Sect. A **594**, 339 (2008).

[27] B. Hoistad, J. Ritman, *et al.*, Proposal for the wide angle shower apparatus (WASA) at COSY-Juelich - "WASA at COSY", arXiv:nucl-ex/0411038.

[28] B. Kłos *et al.*, Experimental study of three-nucleon dynamics in the dp breakup reaction, Few-Body Syst. **65**, 21 (2024).

[29] P. Vlasov, Analysis of the $\eta \to 3\pi^o$ decay in the pp interaction, Ph.D. thesis, Ruhr - Universitat Bochum, Germany, 2008.

[30] A. Ramazani-Moghaddam-Arani, Cross section and analyzing power measurements in three and four-nucleon scattering, Ph.D. thesis, RUG, 2009.

[31] K. Ermisch, H. R. Amir-Ahmadi, A. M. van den Berg, R. Castelijns, B. Davids, E. Epelbaum, E. van Garderen, W. Glöckle, J. Golak, M. N. Harakeh, M. Hunyadi, M. A. de Huu, N. Kalantar-Nayestanaki, H. Kamada, M. Kis, M. Mahjour-Shafiei, A. Nogga, R. Skibiński, H. Witała, and H. J. Wörtche, Systematic investigation of the elastic proton-deuteron differential cross section at intermediate energies, Phys. Rev. C **68**, 051001 (2003).

[32] K. Ermisch, H. R. Amir-Ahmadi, A. M. van den Berg, R. Castelijns, B. Davids, A. Deltuva, E. Epelbaum, W. Glöckle, J. Golak, M. N. Harakeh, M. Hunyadi, M. A. de Huu, N. Kalantar-Nayestanaki, H. Kamada, M. Kiš, M. Mahjour-Shafiei, A. Nogga, P. U. Sauer, R. Skibiński, H. Witała, *et al.*, Systematic investigation of three-nucleon force effects in elastic scattering of polarized protons from deuterons at intermediate energies, Phys. Rev. C **71**, 064004 (2005).

[33] K. Kuroda, A. Michalowicz, and M. Poulet, Mesure de la section efficace differentielle de diffusion proton-deuton a 155 MeV, Phys. Lett. **13**, 67 (1964).

[34] R. Machleidt, F. Sammarruca, and Y. Song, Nonlocal nature of the nuclear force and its impact on nuclear structure, Phys. Rev. C **53**, R1483 (1996).

[35] R. Machleidt, High-precision, charge-dependent Bonn nucleon-nucleon potential, Phys. Rev. C **63**, 024001 (2001).

[36] S. A. Coon and W. Glöckle, Two-pion-exchange three-nucleon potential: Partial wave analysis in momentum space, Phys. Rev. C **23**, 1790 (1981).

[37] R. B. Wiringa, V. G. J. Stoks, and R. Schiavilla, Accurate nucleon-nucleon potential with charge-independence breaking, Phys. Rev. C **51**, 38 (1995).

[38] V. G. J. Stoks, R. A. M. Klomp, C. P. F. Terheggen, and J. J. de Swart, Construction of high-quality *NN* potential models, Phys. Rev. C **49**, 2950 (1994).

[39] A. Deltuva, K. Chmielewski, and P. U. Sauer, Nucleon-deuteron scattering with Δ-isobar excitation: Chebyshev expansion of two-baryon transition matrix, Phys. Rev. C **67**, 034001 (2003).

[40] L. Girlanda, A. Kievsky, and M. Viviani, Subleading contributions to the three-nucleon contact interaction, Phys. Rev. C **84**, 014001 (2011).

[41] L. Girlanda, A. Kievsky, and M. Viviani, Erratum: Subleading contributions to the three-nucleon contact interaction [Phys. Rev. C 84, 014001 (2011)] Phys. Rev. C **102**, 019903(E) (2020).

[42] L. Girlanda, A. Kievsky, M. Viviani, and L. E. Marcucci, Short-range three-nucleon interaction from $A = 3$ data and its hierarchical structure, Phys. Rev. C **99**, 054003 (2019).

[43] H. Witała, J. Golak, and R. Skibiński, Significance of chiral three-nucleon force contact terms for understanding of elastic nucleon-deuteron scattering, Phys. Rev. C **105**, 054004 (2022).

[44] H. Witała, J. Golak, R. Skibiński, and K. Topolnicki, Perturbative treatment of three-nucleon force contact terms in three-nucleon Faddeev equations, Few-Body Syst. **62**, 23 (2021).

[45] H. Witała, J. Golak, and R. Skibiński, Efficient emulator for solving three-nucleon continuum Faddeev equations with chiral three-nucleon force comprising any number of contact terms, Eur. Phys. J. A **57**, 241 (2021).

[46] H. Witała, J. Golak, R. Skibiński, K. Topolnicki, E. Epelbaum, H. Krebs, and P. Reinert, Comprehensive investigation of the symmetric space-star configuration in the nucleon-deuteron breakup, Phys. Rev. C **104**, 014002 (2021).

[47] B. Klos, WASA-at-COSY Collaboration, "Differential cross section for the dp breakup reaction at 190 MeV/nucleon", RepOD, V1, 2026, https://doi.org/10.18150/BAAWZU.